The Role of Mesoscale Convective Systems in Precipitation in the Tibetan Plateau region

Julia Kukulies[1], Deliang Chen[1], Julia Curio[1]

[1]Regional Climate Group, Department of Earth Sciences, University of Gothenburg, Gothenburg, Sweden

Key Points:

- Mesoscale convective systems were tracked in the Tibetan Plateau region for the past two decades
- Co-locations of brightness temperatures with precipitation indicate reduced numbers of mesoscale convective systems over the Tibetan Plateau
- Precipitation and large-scale environments associated with mesoscale convective systems were compared between different subregions

Corresponding author: Deliang Chen, `deliang@gvc.gu.se`

Abstract

Mesoscale convective systems (MCSs) have been identified as an important source of precipitation in the Tibetan Plateau (TP) region. However, the characteristics and structure of MCS-induced precipitation are not well understood in this location. Infrared (IR) satellite imagery has been used for MCS tracking, but cirrus clouds or cold surfaces can lead to false MCS classification over mountain regions. Here, we combine brightness temperatures from IR imagery with satellite precipitation estimates from GPM IMERG and track MCSs over the TP, at the boundary of the TP (TPB), and in the surrounding lower-elevation plains (LE), between 2000 and 2019. In most parts of LE and TPB, MCSs produced 50 to 80 % of the total summer precipitation (60 to 90% of summer heavy precipitation), whereas MCSs over the TP account for below 10 % of the total summer precipitation (10 to 30 % of summer heavy precipitation). Our results also show that MCSs that produce the largest amounts of heavy precipitation are characterised by longevity and large extents rather than by high intensities. These are mainly located in the populous areas south and east of the TP. A tracking of meso-β convective systems over the TP shows that small-scale convection makes a large contribution to total and heavy precipitation. This suggests that more localised convective systems are important for the regional water cycle over the higher terrain and highlights the importance of convective-scale modelling to improve our understanding of precipitation dynamics in the TP region.

Plain Language Summary

Storm systems that extend over several hundred kilometres can represent a risk to people's lives and livelihoods, as they may lead to flooding, extreme winds and heavy rainfall. The Tibetan Plateau (TP) has received increasing attention over the last few decades because it has experienced drastic changes in the water cycle as a response to global warming. Although it is known that large storm systems develop in the populous surrounding regions of the TP, the rainfall characteristics from these storms are not well understood. It is difficult to identify storm systems in satellite images over high mountain regions, because high clouds and low surface temperatures can give signals similar to those of storm clouds. We therefore used a new method to track large storm systems in satellite images over the TP to clarify their role in the water cycle. Our results show that most of the storms that produce heavy rainfall occurred in the regions south and east of the TP. Storm systems over the TP are generally smaller in size and shorter in duration, which means that climate model simulations at high spatial resolution are needed to further investigate them.

1 Introduction

Mesoscale convective systems (MCSs) are organised convective storm complexes, which extend over several hundreds of kilometres and produce large areas of convective and stratiform precipitation (Houze, 2004). MCSs have more complex dynamics than unicellular convective storms, but are primarily defined by their spatial extent (Houze Jr, 2004). Many different forces can drive mesoscale organisation of convection. Thus, the structure and precipitation characteristics of MCSs can take different forms depending on the region of genesis and underlying processes. In the continental mid-latitudes, MCSs often occur in areas downstream regions of high-altitude regions, as MCS formation is related to mountain flow dynamics. On the leeside of the Rocky Mountains (over the Great Plains) (Hitchcock et al., 2019; Cheeks et al., 2020; Hu et al., 2020), in the West-African Sahel (Redelsperger et al., 2002; Vondou et al., 2010; Klein et al., 2018) and in the European Alps (Morel & Senesi, 2002; Feidas, 2017), MCSs produce a significant portion of the total precipitation in a season and can lead to severe weather.

The Tibetan Plateau (TP) covers an area of two and a half million square kilometres and is the world's most extensive mountain region. The headwaters of most of Asia's major rivers are located in the mountains of the TP, and their discharge regimes are mainly controlled by monsoonal precipitation (Zhang et al., 2013). A distinct characteristic of the TP is its high elevation and steep topography, which results in complex interactions between local mountain features and large-scale atmospheric dynamics. Many studies have identified MCSs as one of the most important precipitation-producing mechanisms over the TP (Tao & Ding 1981; Wang et al., 1987; Li et al., 2008; Sugimoto & Ueno, 2010; Hu et al., 2017). Some extreme rainfall and flood hazards in the heavily populated downstream regions to the south and east of the TP have been attributed to MCSs, as have mesoscale vortices that form over the TP (Yasunari & Miwa, 2006; Shi et al., 2008; Xiang et al., 2013; Rasmussen & Houze, 2012). This demonstrates that MCSs can pose a direct threat to life, people's livelihoods, crop yields and infrastructure. On the other hand, MCSs play an important role in the hydrological cycle, as they may account for a significant amount of the annual or seasonal rainfall, for example in North America (Fritsch et al., 1986; Feng et al. 2021). Convection-permitting model simulations project increases in MCS intensity for some regions (Prein et al., 2017; Fitzpatrick et al., 2020) and convective precipitation is likely to increase at much larger rates than a precipitation increase of 7 % per degree of warming, which would correspond to the Clausius-Clapeyron relation (Berg et al., 2013; Ban et al., 2015). It is therefore crucial that we understand the scales and formation processes of heavy precipitation, particularly for mountain regions like the TP, which are likely to experience drastic environmental changes due to global warming (Bibi et al., 2018; Yao et al., 2019).

Although many studies on convection in the TP region focus on MCSs, the main drivers behind the systems and their significance for current and future precipitation regimes are not well understood. It is not clear how characteristics of MCSs that are generated over the TP differ from those of monsoon-related convective systems that occur along the Himalayas (Houze et al., 2007; Romatschke et al., 2010). A number of studies that investigated MCSs at elevations higher than 3,000 m above sea level (a.s.l.) have identified the central and eastern parts of the TP as the main source regions for convection (Jiang et al. 2002; Li et al. 2008; Sugimoto & Ueno, 2010; Hu et al., 2017). However, due to the difficulty in attributing precipitation events to specific storm systems, the importance of MCSs for precipitation could only be roughly estimated. Radar observations of clouds over the southern Himalayas show clear signatures of convection (Houze et al., 2007) with high radar reflectivities over a height range between 5 and 14 km a.s.l. during summer (Kukulies et al., 2019). This may indicate organised convection in this region, but the poor temporal resolution and spatial coverage of spaceborne radar observations raise the question of whether this feature really can be attributed to MCSs or if it derives from isolated deep convection. Additionally, convective cells can be misclassified when infrared (IR) satellite imagery is used to track MCSs in a high mountain region and image scenes include cold cirrus cloud tops (Rossow & Schiffer, 1999; Yuan & Houze, 2010) or cold surfaces under clear-sky conditions that result in a similar IR brightness temperature (Esmaili et al., 2016). Observation-based studies of MCSs are therefore more limited than model studies for the TP region and often cover only a few years, because high-resolution satellite records of more than a decade in length have only recently become available. It is crucial that we establish an accurate climatology of MCSs and understand their importance for precipitation, in order to advance our knowledge about precipitation dynamics in the TP region and to evaluate how well MCSs characteristics are represented in regional climate model simulations. The effect of MCSs on precipitation is key to an improved understanding of the drivers and scales of heavy precipitation which in turn is necessary for more accurate estimates of future changes of precipitation regimes and extreme events.

This study aims to describe MCS characteristics in the TP region using a novel tracking method to interpret satellite observations covering the past two decades (i.e. from

2000 to 2019). To provide a broad overview of different types of MCSs, we compare MCSs over the TP with MCSs that cross the TP boundary (TPB) and MCSs that develop over the surrounding lower-elevation (LE) regions. We focus on the structure and characteristics of MCS-induced precipitation, the contribution of MCSs to seasonal and heavy precipitation as well as the large-scale environments that are associated with different MCS types.

We have organised this paper into four further sections. In Section 2, we compare MCS tracking methods of previous studies and describe the tracking algorithm and datasets used in this study. We also briefly explain the implementation of different MCS standards, to test the sensitivity of the tracking to different thresholds and criteria. In Section 3, we present a comparison of the different tracking methods and an overview of the spatial and temporal characteristics of MCS tracks as well as their precipitation features and associated large-scale atmospheric conditions. Section 4 discusses the role of MCSs in precipitation, retrieval uncertainties and possible driving mechanisms for MCS formation. Finally, a summary and the main conclusions are given in Section 5.

2 Data and Methods

2.1 Previous MCS studies

One of the most commonly used methods to identify MCSs is to detect contiguous areas of brightness temperature minima in IR satellite imagery. A specific type of MCS is a so-called mesoscale convective complex (MCC), originally defined by Maddox (1980). MCCs are cloud systems with a contiguous area of at least 100 000 km^2, within which the maximum temperature is -32°C (241 K) and which includes a region of at least 50,000 km^2, within which the maximum temperature is -52°C (221 K). An additional criterion is that these two conditions must persist for at least six hours for an MCC to be identified. Many studies have used a similar approach for global and regional MCS tracking (e.g. Rossow et al., 1999; Zheng et al., 2008; Esmaili et al., 2016; Huang et al., 2018). However, there is a wide range of thresholds used for brightness temperatures and minimum areas, dependent on whether the aim is to capture the entire evolution of the cloud system or focus on the deep convective part.

Table 1 summarises the tracking criteria used in previous studies that focused on MCSs over the TP or in South-East Asia. Brightness temperature thresholds vary between 219 K and 245 K over minimum areas that range from 1,000 km^2 to 50,000 km^2. The highly varying thresholds reflect that there is no common standard for what defines a MCS in this region. Hence, the large differences in the amount of tracked MCSs per year are not only explained by the different domain sizes and time periods, but also by the different criteria chosen to define a MCS (Table 1). Most studies that only focused on the high altitudes of the TP have used minimum extents of $\leq$5,000 km ^{2}. These smaller, and consequently more short-lived, systems correspond to the meso-β scale (horizontal dimensions of 20 to 200 km) according to the definition of Orlanski (1975), whereas the tracking studies that focused on larger areas in South-East Asia were predominantly designed to identify MCSs at the meso-α scale (horizontal dimensions 200 to 2,000 km).

Some of the studies listed in Table 1 have used global databases for convection tracking (e.g. Li et al., 2008) or thresholds that are also used in global analyses for MCS identification (Guo et al., 2006). However, using universal thresholds can be problematic in a mountain environment like the TP, where low surface temperatures from high mountain tops can be confused with high cloud tops from deep convective clusters, particularly at night and during winter. This has, for example, been discussed in Esmaili et al. (2016), who presented a global cloud cluster tracking with unrealistically high amounts of convective cloud clusters over the TP during winter when only brightness temperatures are used. The atmospheric transmittance at wavelengths corresponding to the IR channels used for tracking ($\sim 10.8\ \mu$m) is relatively high, while surface emissivity at these wavelengths is generally low for dry regions (Schädlich et al., 2001). This means that retrieved clear-sky brightness temperatures are on average lower than the actual surface temperatures, which poses an additional risk of confusing cold surfaces with high cloud tops in dry high-altitude regions.

Table 1. Comparison of different MCS tracking methods used for East Asia and the TP region

Region	Period	Threshold	Extra criterion	Min Extent	Min duration	Reference	Tracks/year (season)
80–105°E, 27–40°N	1998	241 K		1000 km^2	3 h	Guo et al. (2006)	749 (Jun-Aug)
75–105°E, 25–40°N	1998-2001	245 K	221 K cold core	27,000 km^2	-	Li et al. (2008)	160 (Jun-Aug)
80-145 °E,10-55° N	1996-2006	221 K		50,000 km^2	-	Zheng et al. (2008)	-
70–103°E, 29–40°N > 3500 m	1998-2006	219 K		4,000 km^2	6 hrs	Sugimoto and Ueno (2010)	290
75–105°E,25–40°N > 3,000 m	1998-2004	245 K	optical depth $\leq$ 23	25,000 km^2	3 hrs	Hu et al. (2016)	106 (Jun-Aug)
106–113°E, 28–35°N	2000-2016	221 K no 2005		5,000 km^2	3 hrs	Yang et al. (2019)	20 (May-Aug)
80–150°E, 0–55°N	2016	235 K	max area =160 000 km^2	10,000 km^2	3 hrs	Chen et al. (2019)	41,334 (Apr-Sep)
75–103°E,26–40°N > 3,000 m	2000 - 2016 no 2005	221 K		5,000 km^2	3 hrs	Mai et al. (2021) (May-Sep)	609
102.58–121.58°E, 21.08–38.08°N	2008 - 2016	3 mm h^{-1}		3,600 km^2	6 hrs	Li et al. (2020)	420 (Mar-Nov)
105-123°E,28-35°N 105°-123°E,20-27°N	2014 - 2018	241 K	225 K cold core	60 000 km^2	6 hrs	Cui et al. (2020)	30 (May-Sep)

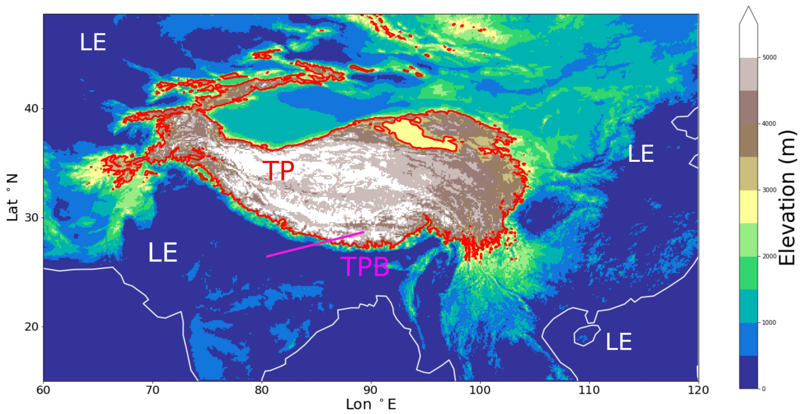

Figure 1. Study area (15 – 50 °N, 60 – 120 °E) for regional MCS tracking. The colours show elevations [m a.s.l.] and the red line indicates the 3,000 m boundary of the TP. MCSs are divided into systems located outside of this boundary (LE), systems over the TP, and systems which cross the 3,000 m boundary during their lifetime (TPB).

Another risk of exclusively using IR brightness temperatures as a proxy for convective activity in mountain regions is that convective systems can also be confused with cirrus or stratiform cloud shields that are not necessarily the remnants of a storm system. Kukulies et al. (2019) found that cirrus clouds are among the most frequent cloud types over the central and southern parts of the TP between May and September. Thus, it is likely that these cloud shields do not always originate from old convection. The high number of MCS tracks that has been identified by Chen et al. (2019) (Table 1) reveals, for instance, potential issues when the brightness temperature threshold is set too low and when no additional data or criteria are used to assure that the low brightness temperatures are linked to deep convection. To address the above-named issues, we followed a similar approach to Feng et al. (2021) who created an updated global MCS dataset based on an objective tracking method that combines IR imagery with precipitation data and therefore reduces misclassifications of MCSs attributable to cirrus cloud layers and cold surfaces.

2.2 Data and Tracking algorithm

Figure 1 shows the domain (15 – 50 ° N, 60 – 120 °E) in which the MCS tracking was performed. The study area encompasses regions with substantially different precipitation regimes, such as the Indo-Gangetic Plain, which is dominated by frequent monsoon depressions (Hurley & Boos, 2015; Boos et al., 2017) and the generally drier TP. Considering such a wide area with diversified background climates, this study provides a regional overview of MCSs, allowing those over the TP to be compared with those that are initiated over more populous areas in the downstream regions. In this study, we therefore distinguish between three main types of systems: MCSs and precipitation events that are initiated within the 3,000 m boundary of the plateau (TP), MCSs that cross the 3,000 m elevation boundary during their lifetime (TPB), and MCSs and precipitation events at lower elevations (LE), outside the 3,000 m boundary (Fig. 1).

We used half-hourly satellite precipitation estimates from the Global Precipitation Measurement Mission (GPM) in combination with brightness temperatures from IR imagery. The merged and angle-corrected brightness temperatures used in this study are provided by NCEP/CPC (National centres for Environmental Prediction/Climate Prediction centre) and were acquired by various sensors on board Meteosat, GMS/Himawari, Meteosat and GOES (Janowiak et al., 2017). The dataset can be downloaded from the data provider NASA GES DISC at 30 min resolution and with 4 km grid spacing. In order to obtain the same spatial resolution as the satellite precipitation data product GPM IMERG V06 (Huffman et al., 2019), which has a spatial resolution of 0.1 °. To facilitate co-locating the two datasets, we regridded the brightness temperature data to match the GPM IMERG grid using first-order conservative mapping with the software Climate Data Operators (`https://code.mpimet.mpg.de/projects/cdo`). The tracking was performed in 30 min time steps to match the original temporal resolution of both datasets, for the period 2000 to 2019.

The tracking procedure consists of three main steps: 1) cloud feature detection using IR brightness temperatures, 2) linking of cloud features over time and 3) applying additional criteria based on co-locations with precipitation. Using the python package *tobac* (Heikenfeld et al., 2019), cloud features were identified in each time step in the regridded field of IR brightness temperatures (T_b). The tracking library allows for smoothing the input field using a Gaussian filter. However, after testing different smoothing options, we set the Gaussian filter to 0.5, which results in a minimal smoothing of the brightness temperatures and keeps the details of the cloud structure in the original data. To detect cloud features, we adapted the brightness temperature threshold of 221 K used in the original paper by Maddox (1980) and more recently in the same study region by Zheng et al. (2008). Because the focus of this paper is on MCSs with potentially large impacts on surface precipitation, we performed a tracking at the meso-α scale that requires a minimum cloud area of 50,000 km^2. A cloud feature is hence defined as a contiguous area over 50,000 km^2 with brightness temperatures $\leq$ 221 K. In summer, cloud top temperatures below 221 K correspond to cloud top heights of about 10 km a.s.l. over the TP (Chen et al., 2018), which let us assume that brightness temperatures below this threshold are likely to be associated with deep convection at least during the warm season.

Once cloud features have been identified in each time step, these features were linked over time based on their location and propagation speed. This was done by predicting the location of the cloud feature in the next time step using its average propagation speed from the previous time steps (or the average propagation speed of the closest feature for the first time step). Potential features within a restricted radius around the predicted location were then identified and the closest feature was connected with the trajectory, if its location was within a realistic distance to the previous cloud feature. More details about this linking method can be found in Heikenfeld et al. (2019). To be retained as a potential MCS, the minimum area of 50,000 km^2 has to persist for at least 3 hours (6 time steps). Due to limited computational resources the feature linking was performed on yearly aggregated files, which means that MCSs at the boundary between two years appear as separate tracks. However, this does not significantly affect the results, since most MCSs in the study region occur during the summer season (see Section 3.2). It should also be noted that the merging and splitting of MCSs does not have any explicit treatment in the algorithm, but results in the survival of the MCS with the most similar travel direction (Heikenfeld et al., 2019). This way, we can identify long-lived MCSs that grow upscale when multiple cells merge into one larger MCS.

To assure that identified cloud features are indeed precipitation-producing systems with a region of deep convection, we filtered the connected cloud features based on two additional criteria that have been suggested by Yuan and Houze (2010) and Chen et al. (2018): the presence of a cold core reflected by an even higher temperature threshold within the cloud feature and the presence of heavy rainfall during the MCS lifetime. To be classified as a MCS, brightness temperatures had to drop below 200 K (as in Yuan and Houze

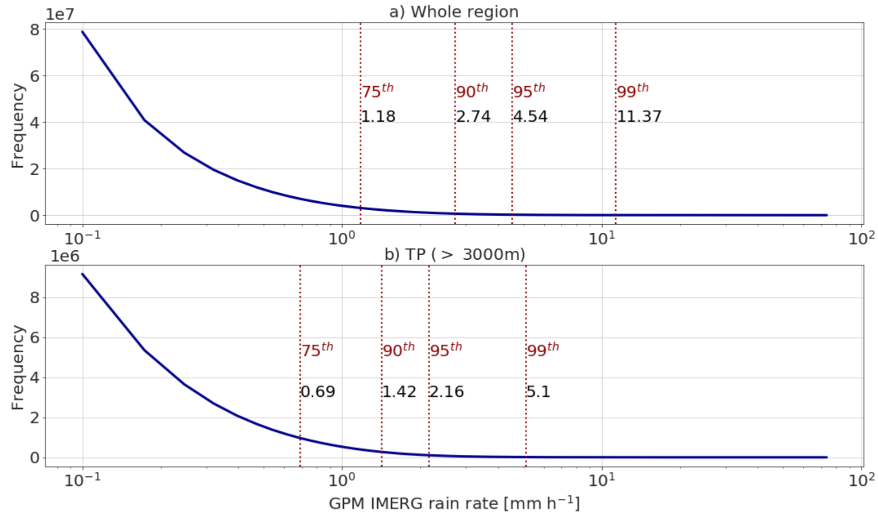

Figure 2. PDF and percentiles of hourly rain rates from GPM IMERG v06 2000 - 2019 for a) the whole study area (15 – 50 ° N, 60 – 120 °E) and b) the TP > 3,000 m a.s.l.

(2010)) and contain an area that is at least 10 % of the minimum cloud area threshold of 50,000 km^2 (or 5,000 km^2 for meso-β) with rain rates above 5 mm h^{-1} once during the MCS lifetime (as in Chen et al. (2018)). The precipitation threshold was chosen based on the evaluation of the probability density function (PDF) of IMERG precipitation pixels in the study region. The PDF shows that a rain rate of 5 mm h^{-1} corresponds approximately to the 95th percentile of all hourly rain rates (Fig. 2).

In summary, a MCS in this paper is defined as a contiguous area of $\leq$ 221 K over at least 50,000 km^2 that persists for at least 3 hours, develops an area below 200 K and a precipitating area with rain rates $\geq$ 5 mm h^{-1}). The tracking procedure and criteria are visualised in Figure 3. If the cloud feature in one time step does not fulfil the minimum area and brightness temperature criteria anymore, it is regarded as dissipated.

We also performed a meso-β tracking over the TP that requires an area of at least 5 000 km^2 below the same threshold (221 K), as suggested in Mai et al. (2021). These systems are referred to as TCSs (Tibetan Convective Systems) and be used to discuss small-scale convective systems in the mountainous region. Systems that grow into meso-α systems at a later stage are excluded from this subgroup, so that the characteristics of systems that do not grow larger than meso-β scale can be compared to the systems from the meso-α tracking. The meso-β tracking is hence limited to systems that develop *at most* dimensions at the meso-β-scale, whereas the meso-α tracking contains MCSs that grow upscale (which means that these may have been meso-β systems before they reached meso-α dimensions). The purpose of tracking cloud features at two different spatial scales is to investigate the role of convective systems at the lower bounds of the mesoscale over the TP compared to larger MCSs. Due to limited computational resources, the meso-β tracking could not be implemented for the entire study area as it would result in too many cloud feature combinations that had to be assessed to determine linkages across time steps. In the surrounding downstream regions, the focus is thus on convective systems at the meso-α scale, which we assume are more important for severe events and interactions with the large-scale atmospheric circulation.

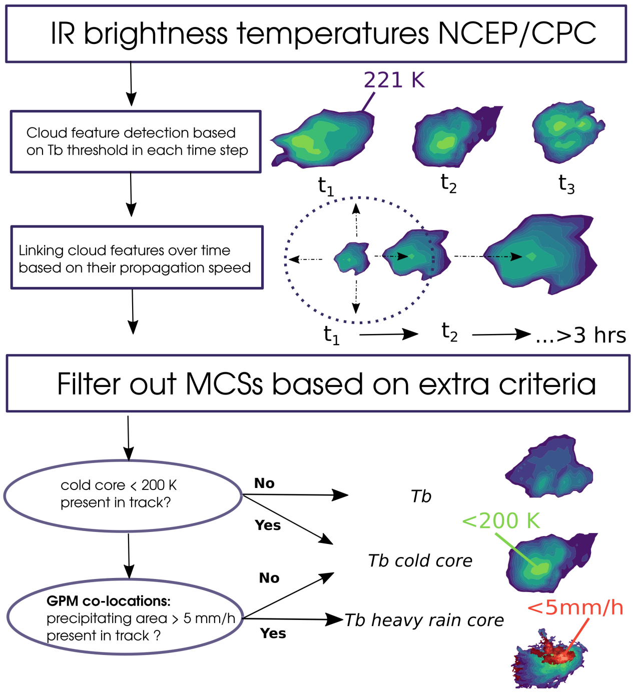

Figure 3. Flow chart and visualisation of MCS tracking procedure and criteria.

2.3 Analysis of MCS types and associated precipitation features

All tracked MCSs were assigned to one of four classes based on their dominant propagation direction (eastward or westward) and genesis location. These are denoted as TPB + TP east, TPB + TP west, LE east and LE west, where TPB + TP refers to MCSs over and at the boundary of the TP and LE refers to systems in the lower elevated surrounding regions that do not cross the 3,000 m boundary of the TP during any stage in their lifetime (Fig. 1). TP systems are defined as MCSs that have their cloud feature (221 K contour) within the 3,000 m boundary in the first detected time step, whereas TPB systems are defined as MCSs that show at least one time step where more than half of the cloud feature is located within the 3,000 m boundary. We focus on east-moving and west-moving systems because these were the two dominant propagation directions. East-moving MCSs reflect the transport of weather systems by mid-latitude westerlies and the other propagation directions result from an interaction between westerlies, the southerly Indian summer monsoon circulation and the easterly flow of the East Asian Monsoon. The propagation directions were determined using least-square fitting of all centre locations that belong to the same MCS track, so that MCSs that move along curved lines are assigned to the direction of their regression line.

The motivation for separating MCS trajectories into TPB + TP and LE was to distinguish between MCSs that originate at higher elevations and/or interact with the topography compared with MCSs in the plains. We used the cloud feature characteristics at each time step (area, brightness temperature intensity, precipitation features) and the characteristics of the track that describe the MCS evolution (lifetime, total precipitation, total heavy precipitation, propagation direction) to compare the different MCS types. Since the python package *tobac* allows for feature tracking using multiple thresholds, each identified cloud feature was also assigned to an intensity category (see Section 3.3.3). The intensity categories are defined as contiguous areas within the detected cloud feature where a specific brightness temperature threshold is exceeded (between 190 K and 221 K).

To investigate the importance of MCS-associated precipitation for the water cycle, the total amount of precipitation was calculated for each of the detected cloud features and compared to the total seasonal precipitation received in each grid cell for the period 2000 to 2019. An MCS-associated precipitation feature is defined by all matched precipitation pixels within the detected cloud feature. We also included contiguous precipitation up to 1.0 mm h^{-1} outside of the cloud feature when it was directly connected to the main precipitation feature, in order to take account of stratiform precipitation behind or around the convective core. Because other precipitation-forming mechanisms than MCSs may dominate the total annual and seasonal precipitation in some subregions, we also examined the importance of MCS-associated rainfall for heavy precipitation events only. The range of rainfall intensities that are typically used to classify convective precipitation is wide (Gaál et al., 2014) and what can be called heavy or extreme precipitation depends on the regional conditions. After the evaluation of the PDF of hourly rain rates estimated by GPM IMERG (Fig. 2), we refer to heavy precipitation in the study region as precipitation produced by rain rates exceeding 5 mm h^{-1}. This rain rate threshold corresponds to the 99^{th} percentile of rain rates over the TP and to the 95^{th} in the surrounding monsoon-affected areas in the GPM IMERG dataset.

2.4 Sensitivity tests

It is important to note that the atmospheric variable selected as a proxy for storms and convection (e.g. brightness/cloud top temperature, outgoing longwave radiation, precipitation, vorticity or geopotential) determines the spatial and temporal characteristics of the tracked MCSs. There are many advantages to using precipitation, as it is a key component in the water cycle that has direct impacts on hydrology and society. It is also straightforward to compare precipitation tracks with model and reanalysis data, whereas IR brightness temperatures as seen by satellites are usually not available as a standard output variable from models. However, the part of a MCS in which precipitation is produced is usually smaller and more short-lived than the cloud system as a whole. Hence, using precipitation as a proxy for convection provides a more limited view of both the structure and evolution of tracked storm systems compared to brightness/ cloud top temperature.

To understand the implications of different MCS tracking methods on the key statistical features, we tested our tracking with four different methods. First, we performed tracking using only brightness temperatures (T_b) with the temperature threshold of 221 K for the cloud feature identification. We then added the cold core criterion (T_b *cold core*) and the heavy rain criterion (T_b *heavy rain core*) that were described in Section 2.2. The MCS criteria for each tracking method are also summarised in Figure 3.

We also tested the sensitivity of the minimum area threshold for the heavy rain core, but no significant differences could be detected between 1 and 25 grid cells. Finally, we also implemented a tracking based on precipitation only, following the criteria used in Li et al. (2020) with minimum rain rates of 3 mm h^{-1} over a minimum area of 3 600 km^2 persisting for at least 6 hours (*Precip*). Considering the PDF of rain rates in the TP region compared to the surroundings (Fig. 2), this threshold represents a reasonable compromise to track precipitation cells in the more humid parts of the study domain as well as over the drier TP.

Table 2 summarises the criteria of the four different methods for the meso-α and meso-β tracking as well as the number of MCSs identified in each tracking. The tested criteria are the same for the meso-β tracking over the TP, to check whether the effect of the criteria also depends on region and scale. The number of MCS tracks in Table 2 is substantially higher when only precipitation cells are tracked (*Precip*) than for the other

Table 2. Criteria and total number of tracks for different tracking methods from 2000 to 2019

Test	Threshold	Extra criterion	Min extent [km^2]	Min time [hrs]	MCS tracks [avg per year]
meso-α tracking					
T_b	$\leq$ 221 K		50,000	$\geq$ 3	1,787
T_b *cold core*	$\leq$ 221 K	200 K	50,000	$\geq$ 3	1,305
T_b *heavy rain core*	$\leq$ 221 K	10% > 5 mm h^{-1}	50,000	$\geq$ 3	1,267
Precip	$\geq$ 3 mm h^{-1}		3,600	$\geq$ 6	4,680
meso-β tracking					
T_b	$\leq$ 221 K		5,000	$\geq$ 3	1,283
T_b *cold core*	$\leq$ 221 K	200K	5,000	$\geq$ 3	447
T_b *heavy rain core*	$\leq$ 221 K	10% 5 mm h^{-1}	5,000	$\geq$ 3	429

tracking methods. However, as will be shown in more detail in the next section, the area distribution of the precipitation cells reveals much smaller spatial extents. Furthermore, because tracked precipitation events are not always as continuous in time and space as in the clearest cases of well-developed MCSs, the tracking results in many more individual cells. The additional criteria result in fewer MCS tracks compared to the T_b tracking, meaning that there are large cloud clusters > 221 K that do not produce precipitation (Table 2). This effect is particularly visible for the meso-β tracking that has been limited to the TP, presumably due to the previously mentioned concerns regarding cold surfaces and cirrus clouds (see Section 2.1). Interestingly, the difference in the total number of tracks between T_b *cold core* and T_b *rain core* is very small for both the meso-α tracking and meso-β tracking, meaning that the cold core criterion seems to automatically assure that heavy rainfall is produced in most of the identified cloud features. In the next Section, we present more detailed MCS characteristics for each tracking method.

3 Results

3.1 Comparison of tracking methods

Figure 4a exemplifies co-located IR brightness temperatures with GPM IMERG precipitation data for the study area. The snapshot shows a mature MCS on July 20^{th}, 2008 and the succeeding plots show the evolution of the MCS track (Fig. 4b-e). The MCS persisted for 18.5 hours and produced substantial amounts of heavy rainfall in the downstream region to the east of the TP. We used this well-known event, which was likely triggered by a Tibetan Plateau vortex (Curio et al., 2019), as a case study to check whether our tracking algorithm is able to capture the evolution of the system. In this example, the amount of precipitation over time follows approximately the evolution of the cloud area and peaks about six hours after the initiation, just before the cloud area reaches its maximum (Fig. 4g).

For other MCS cases, however, the lifetime of contiguous heavy precipitation may be much shorter than the lifetime of the cloud cluster it is embedded in. As the chosen tracking criteria can have a substantial effect on the main characteristics of a MCS climatology, we summarise the key features of tracked MCSs identified by the four different tracking methods (T_b, T_b *cold core,* T_b *heavy rain core, Precip*) in Figure 5. The high number of *Precip* tracks in each month compared to the other tracking methods can partly be explained by the smaller area threshold that needs to be met (Table 2), but also by the fact that precipitation in a MCS may cease and be re-initiated into the same cloud cluster (Fig. 5a). On top of that, precipitation is not necessarily contiguous in time and space, but can occur as separate cells that are not identified as the same system in the *Precip* tracking and hence result in larger numbers of individual tracks. The main difference between T_b compared to T_b *cold core* and T_b *heavy rain core* is the higher number of tracks for T_b that are identified between January and April. This can mainly be attributed to features over the cold TP that are probably mistakenly identified as MCSs, as shown in Figure 6.

The diurnal cycle for MCSs identified using *Precip* has multiple peaks (Fig. 5b), whereas the other tracking methods are marked by a bimodal distribution with a clear afternoon and a night/early morning peak. This difference in initiation time can also be a side effect from the fact that *Precip* is limited to the MCS features that produce precipitation, while the other tracking methods capture the evolution of the MCSs more completely, including non-precipitating hours. In addition, the *Precip* tracking includes smaller systems, since the area threshold has to be set relatively low, in order to capture most systems that produce a contiguous area with heavy precipitation. Even though we captured *Precip* systems which have on average longer lifetimes than the majority of the cloud cells (Fig. 5c), these have much smaller spatial extents that barely overlap with the MCS area distributions derived from the other three tracking methods (Fig. 5d). The rela-

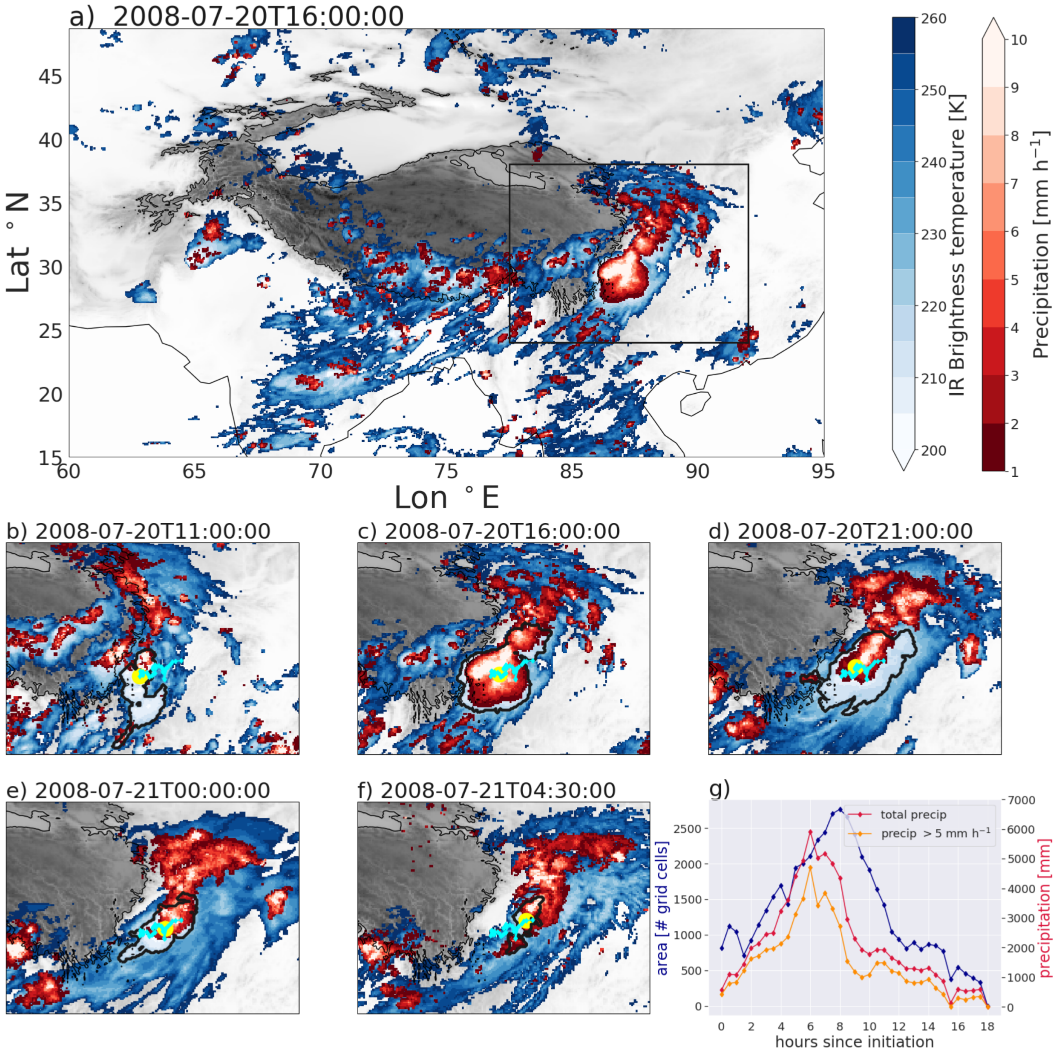

Figure 4. Example of a tracked MCS at the eastern boundary of the TP on 20-21th July, 2008. The upper panel shows a snapshot of half-hourly IR brightness temperatures and GPM IMERG precipitation (a). The evolution of the tracked cloud and precipitation feature are shown in the following panels (b-f), where the black line indicates the MCS centre locations at the preceding and succeeding time steps and the yellow dot marks the MCS centre location in the imaged time step. The evolution of the cloud feature area (blue), total precipitation (red) and total precipitation >5 mm h^{-1} (orange) is shown in the time series graph (g).

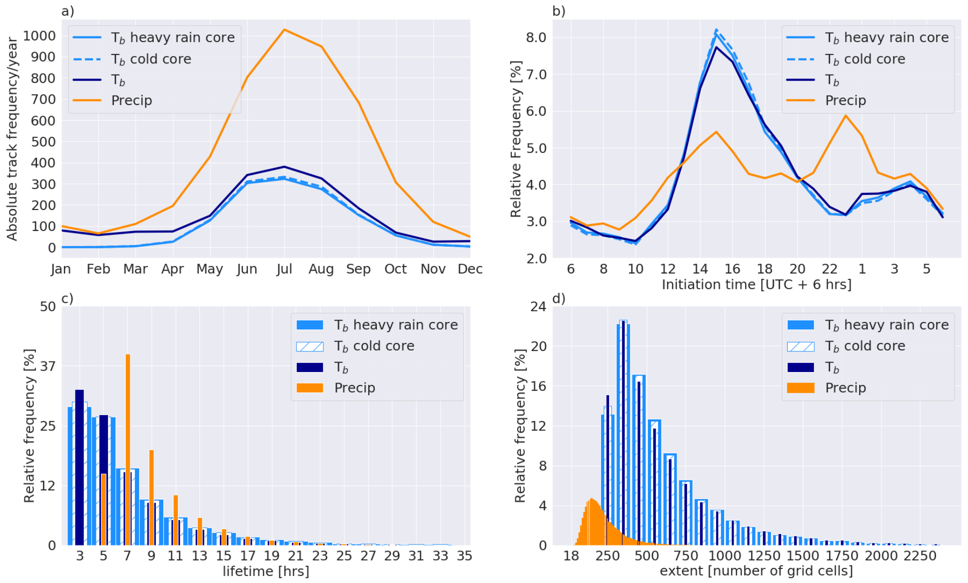

Figure 5. Comparison of characteristics for MCSs identified using four different tracking methods. The histograms show the a) annual cycle of tracks and the relative frequencies [%] for b) initiation time [UTC+6 hrs], c) lifetime [hrs] and d) mean extent [number of grid cells].

tive frequency of systems with spatial extents around the minimum area threshold (250 grid cells) is slightly higher for T_b than for T_b *cold core* and T_b *heavy rain core*, but all three exhibit the largest frequency for systems between 350 and 500 grid cells (Fig. 5d). This horizontal dimension corresponds to an area of about 80 000 km^2 and is thereby close to the extent of a MCC (Maddox, 1980).

Contiguous precipitation cells are less common over high altitudes, which is shown by the results of the *Precip* tracking over the TP that exhibits only a very small number of cells despite the relatively small area threshold (Fig. 6a). The *Precip* tracking could, for instance, miss MCSs that are initiated over the TP (e.g. through Tibetan Plateau vortices (Curio et al., 2018)), but first grow into larger precipitation cells in the moister downstream regions. Additionally, the biases of satellite-derived precipitation estimates over high and complex terrain are only poorly understood, so it is unclear to which extent the detection of contiguous precipitation is influenced by these (see more detailed discussion in Section 4.2). Using precipitation only is therefore less useful to investigate the role of weather systems originating over the mountains that result in organised convection in the downstream regions. We conclude that the combined brightness temperature-precipitation tracking (T_b *heavy rain core*) is clearly advantageous, because it can capture a more complete cloud cell evolution and at the same time the precipitation evolution, which is the most relevant parameter in a MCS.

The difference in total tracks between T_b and T_b *cold core*/T_b *heavy rain core* is even more pronounced for the meso-β tracking over the TP (Table 2), particularly during the winter months (Fig. 6a). The seasonal cycle is clearly influenced by the higher amounts of TCSs between January and April for T_b compared to T_b *cold core*/T_b *heavy rain core* (Fig. 6a). A similar result was observed by Hu et al. (2017), who used MCS data from the global *ISCCP Convective Tracking Database* (Wang et al., 2018) to examine convective systems over the TP. By filtering the tracked cloud features based on an additional threshold for optical depth, they found that the winter maximum for MCS events changed to a summer maximum, which is more consistent with the well-established understanding of summer convection over the TP (Flohn & Reiter, 1968; Ye & Wu, 1998). Hence, the seasonal cycle in Figure 6a shows the effect of falsely classified MCSs over the mountains due to cold surfaces or cirrus clouds which was discussed earlier (see Section 2.1). When precipitation data is used to verify the presence of MCSs, we see a notable reduction of such erroneous MCS classifications during the cold season. This is consistent with the global dataset of Feng et al. (2021), who found a reduction of MCS tracks over the TP by more than 50 %, when applying precipitation-based and brightness temperature-based criteria compared to a tracking based on brightness temperatures only.

In addition, the results of the meso-β tracking show differences in lifetime and spatial extent between T_b and T_b *cold core*/T_b *heavy rain core*, where T_b results in generally more short-lived and smaller cells. This is also in line with our assumption that the wrong cloud features or the background in the mountains are classified as MCSs, because these are most likely less persistent than organised storm systems.

It is worth noticing that T_b *cold core* and T_b *heavy rain core* exhibit the same key characteristics and almost the same number of monthly tracks in both the meso-α (Fig. 5) and the meso-β tracking (Fig. 6). This means that most of the MCSs that develop a rain core with > 5 mm h^{-1} over at least 10 % of the minimum area at least once during their lifetime also exhibit brightness temperatures < 200 K. From this observation, we conclude that the extra criterion for brightness temperatures that assures the development of a convective core is enough to simultaneously assure that the system produces heavy precipitation. Nevertheless, it remains advantageous to include precipitation data in the tracking, in order to derive comparative information on the precipitation features in the identified MCSs.

3.2 Spatial and temporal characteristics

As shown in Figure 7a, most of the TP + TPB systems are initiated in the eastern and southern TP. The Himalayas appear as a separator of MCS tracks, because the low track density along the 3,000 m contour line in the south indicates that only few MCSs can cross the mountain range. Instead, they are blocked by the orographic barrier and produce rainfall over the Indo-Gangetic Plains and at the southern foothills of the Himalayas, where a large amount of rainfall occurs (Kukulies et al., 2020). The same pattern can be seen for TP + TPB west, but with generally smaller numbers of MCS tracks over the TP (Fig. 7b). The highest initiation density of MCSs in the LE region are over the Bay of Bengal for LE east (Fig. 7c) and over the Indian subcontinent for LE west (Fig. 7d).

Figure 8 shows histograms of monthly occurrences (a), initiation time (b), lifetime (c) and mean extent (d) for the MCS types LE west, LE east, TP + TPB west and TP + TPB east. The total number of LE east and LE west are significantly higher than MCSs that interact with the TP (TP + TPB). The maximum occurrence for LE east and TP + TPB systems is in July, when the Indian summer monsoon season over the TP has already started and matured, whereas LE west systems have their maximum in June (Fig. 8a). The MCS season for LE systems is generally more prolonged over the entire monsoon season with relatively high occurrences during May and October, where only very few cases occur for TP + TPB (Fig. 8a).

An interesting feature of the diurnal cycle for MCS initiation is that TP + TPB systems are mostly initiated in the afternoon and nearly never in the morning hours, whereas LE west and LE east are initiated frequently during all hours and exhibit a smaller, less pronounced afternoon peak (Fig. 8b). The second initiation peak during night that is visible for the meso-α tracking (Fig. 5b), disappears in the meso-β tracking (Fig. 6b),

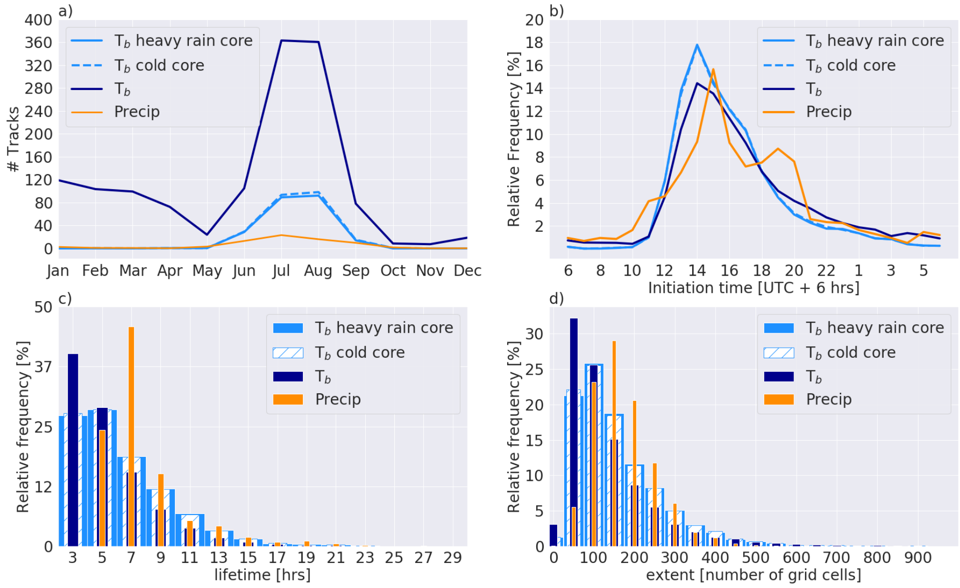

Figure 6. Same as in Figure 4, but for TCSs that were tracked by the meso-β tracking (see Table 2 for criteria). *Precip* is from the same tracking as in Figure 4, but the characteristics are only shown for cells within the 3,000 m boundary of the TP.

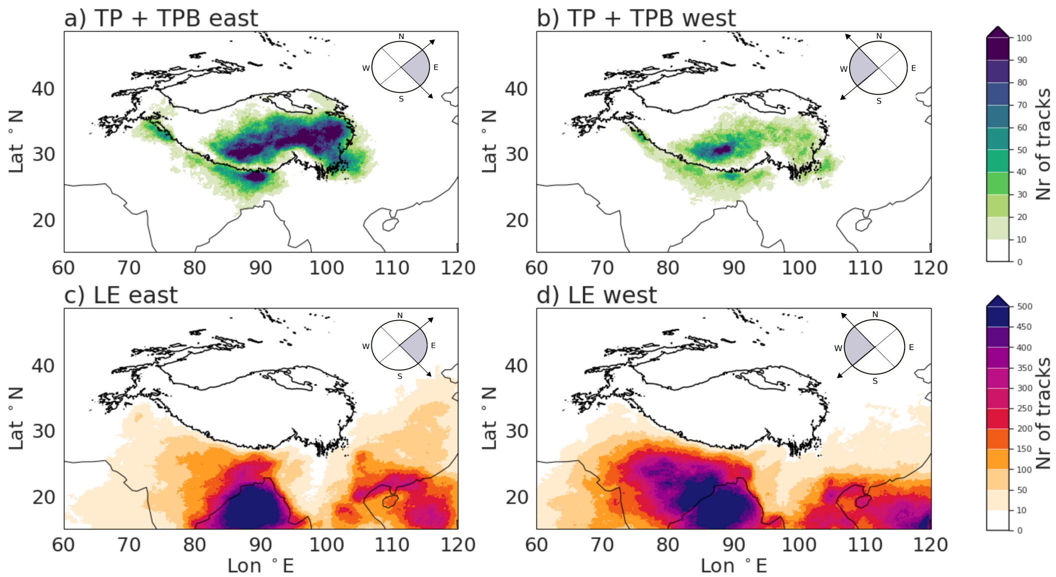

Figure 7. Density of initiation locations for TP + TPB east (a), TP + TPB west (b), LE east (c) and LE west (d). The colour shading shows the total number of MCS cloud features that were detected in each grid cell for the period 2000 to 2019. The grey region in the wind rose in each panel marks the directions that are covered by east-moving and west-moving systems. As shown in the wind roses, 'east' corresponds to directions between 46° and 135° and 'west' to directions between 226° and 314°.

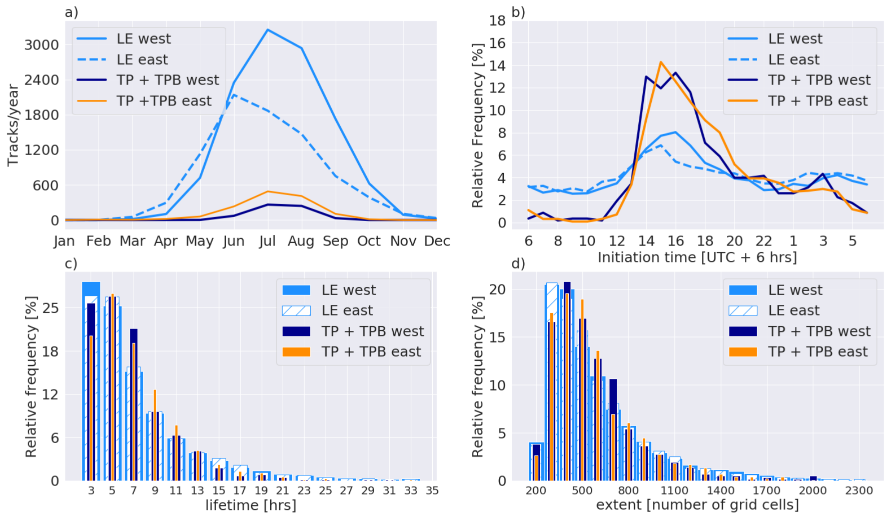

Figure 8. Spatial and temporal characteristics of eastward- and westward-moving MCSs in the LE and TPB regions. The histograms show the absolute occurrences of a) monthly tracks and the relative frequencies [%] for b) initiation time [UTC+6 hrs], c) lifetime [hrs] and d) mean extent [number of grid cells].

which suggests that the interaction with topography plays a crucial role for the initiation time. The distributions of lifetime and mean extent are similar for the four MCS types (Fig. 8c-d), showing that long-lived MCSs and large MCSs are not predominantly attributable to one of the four MCS types, but exist in each subgroup. More than 75 % of the tracked MCSs in each subgroup do not last longer than 12 hours, but all four MCS types also contain extreme cases with MCSs that last longer than 24 hours (Fig. 8c). The distribution of MCS extent is generally right-skewed, similar to the distribution of MCS lifetime, and MCSs with the most extreme extents belong to LE west and LE east (Fig. 8d). Most of the tracked MCSs have a mean extent between 300 and 600 grid cells, which corresponds to an area of about 60 000 – 120 000 km^2. This shows that the area of the cloud shields for most of the systems is slightly larger than the required minimum cold area (Fig. 8d) and that the horizontal dimension of the dominating MCS type in the study area is comparable to *Mesoscale Convective Clusters* (described in Section 2).

It is important to understand the diurnal evolution of MCSs that originate over the TP, because they may be closely linked to topographically-driven diurnal flow patterns. Therefore, we further separate TP + TPB systems into MCSs that are initiated over the TP from systems that are initiated at lower elevations, but interact with the higher terrain (TPB), and compare the temporal evolution of these MCS types with the evolution of LE systems over land and ocean. Figure 9 shows histograms of the hours of the day at which the different MCS types are initiated (when they are first tracked as a cloud feature), reach maturity (the age of a cloud feature when its embedded area of precipitation > 5 mm h^{-1} is greatest) and dissipate (when the area tracked as a cloud feature is last tracked). The first two histograms in Figure 9 refer to a) TP systems that are initiated at high altitudes and b) TCS that were tracked with the meso-β tracking. These two MCS types show the same pattern with a distinct single maximum for initiation in the afternoon, maturity in the evening and dissipation during night. The resulting evening and night peaks in precipitation are consistent with the dominating di-

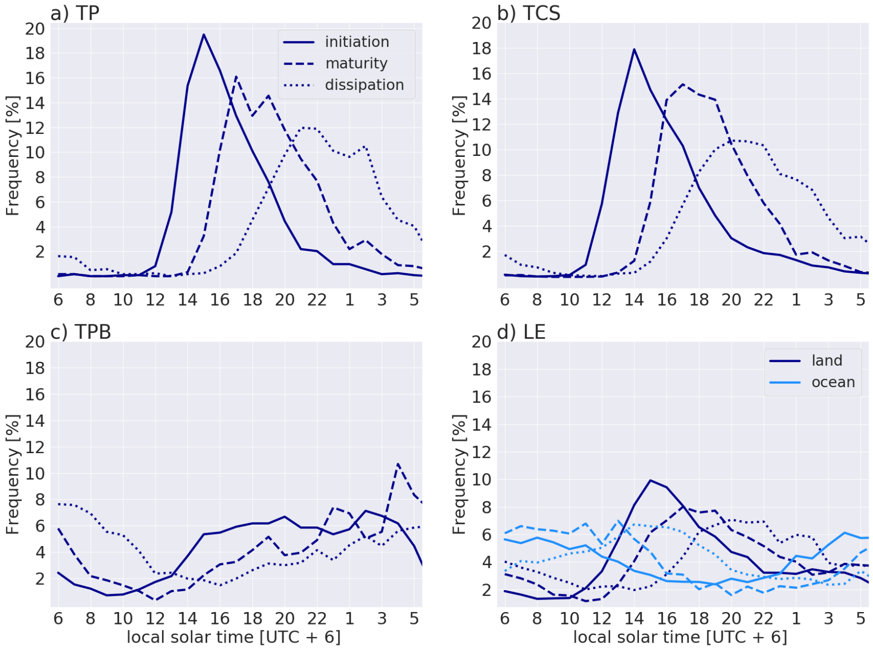

Figure 9. Temporal evolution of a) MCSs that initiated over the TP (1237 cases), b) TCSs (8580 cases) c) TPB (1537 cases) d) LE ocean (8096 cases) and LE land (15019 cases). The histograms show the relative frequencies for the times of the day associated with initiation, maturity (time point with maximum precipitation > 5 mm h^{-1}) and dissipation.

urnal cycle of precipitation over the southeastern TP (W. Xu & Zipser, 2011; Kukulies et al., 2019) and indicate that the diurnal flow has an important effect on mountain convection and the organisation of convective systems into larger systems. The main initiation, maturity and dissipation times for TPB systems exhibit, in contrast, a much larger range (Fig. 9c) with particularly high frequencies for both initiation and maturity during the evening and night hours. The resulting flatter diurnal cycle is more similar to MCSs initiated over the ocean (Fig. 9d), which are generally less affected by the diurnal forcing of surface heating over land. The less pronounced diurnal cycle of TPB systems indicates that the large-scale forcing (e.g. the monsoon flow that brings moist air to the mountains) is a more important factor than the diurnal circulation or that processes with different diurnal cycles lead to MCS formation at the edges of the TP. The high MCS initiation frequencies during night can, for instance, be related to downslope winds as a consequence of nighttime cooling in the Himalayas (Romatschke et al., 2010), whereas MCSs at the more eastern edges of the TP are influenced by other mechanisms. The second peak during night that occurred in the distribution for all MCSs (Fig.8b), can therefore be attributed to LE and TPB rather than to TP systems. LE systems over land have a similar but flatter diurnal cycle compared to TP and TCS (Fig. 9d), which suggests that the difference between LE and TP + TPB systems in Figure 8b is also caused by the large number of MCS tracks over the ocean (Fig. 7). These are not constrained by strong nocturnal cooling as in MCSs over land and can therefore continue to form and develop during the night (Houze, 2004; Huang et al., 2018).

3.3 MCS-associated precipitation

3.3.1 Contribution to total and heavy precipitation

Figure 10 shows the average contributions of precipitation from tracked MCS cloud features to total precipitation and heavy precipitation (where heavy precipitation refers to rainfall events with a rate of at least 5 mm h^{-1}) for each month during the monsoon season (May to September). During the onset of the Indian summer monsoon (May and June), the highest MCS contributions to precipitation are over the ocean (Bay of Bengal, Arabian Sea and South China Sea) and in the coastal regions, where MCSs bring more than 80 % of the total monthly precipitation (Fig. 10a-d). With the progression of the Indian summer monsoon, the MCS fraction of precipitation over the Bay of Bengal decreases to 40 to 60 % in September (Fig. 10i-j). Over land, there is a similar time evolution, with decreasing MCS fractions from the peak month in June. However, in contrast to the development over the Bay of Bengal, MCS contributions over the Indian subcontinent are higher in September than in May.

The regions over land with the highest MCS contributions are the Indo-Gangetic Plains and the Sichuan and Yangtze river Basins, where large areas exhibit more than 50 % MCS-associated rainfall, particularly during the mature phase of the monsoon between June and August (Fig. 10c-h). This regional pattern is consistent with Feng et al. (2021) who suggest that MCS contributions to total annual rainfall are highest over the Bay of Bengal (70 to 80%), above 50 % over large parts of the Indian subcontinent and between 30 and 40 % over most parts of China (Feng et al., 2021). These estimated ranges are very similar to our results which show only a few locations with slightly higher fractions, most likely because we focus on particular months during the monsoon season rather than on total annual precipitation.

In all months, the spatial pattern of MCS contributions is similar for both total and heavy precipitation, but most regions show a slightly higher MCS contribution for heavy precipitation (Fig. 10). The difference between the contributions to total and heavy precipitation is especially pronounced over the eastern parts of the TP (e.g. Fig. 10d, f, h). Over the TP, MCS contributions peak during July, where larger areas in the southern and eastern parts exhibit MCS fractions of 10 % and 20 % to total precipitation and 20 to 50 % to heavy precipitation (Fig. 10e-f). During June and August, the contribution of MCSs is below 20 % for most parts of the TP (Fig. 10c-d, g-h). In May and September, there is almost no MCS-associated precipitation over the TP, except for some small fractions at the eastern edges (Fig. 10a-b and i-j).

The results for the TP are also consistent with the estimations of Feng et al. (2021), but are in contrast with several previous studies that have suggested that MCSs over the TP can explain up to 70 % of the local precipitation during the warm season (Li et al., 2008; Hu et al., 2016). Given that Feng et al. (2021) have taken the same approach as we did, this result suggests once again that considering precipitation during MCS tracking can have a notable effect on conclusions about the role of MCSs in the regional water cycle in mid-latitudinal and alpine climate, where cold cloud tops are not necessarily linked with convective precipitation.

Another reason for the rather low MCS contributions over the TP in comparison with the surrounding downstream regions is the spatial extent of convective systems. In comparison with MCSs, TCSs (Table 2) make a significantly higher contribution to total and heavy precipitation over the high altitudes during the summer months (Fig. 11). These results confirm our hypothesis that precipitation-bearing systems that organize at smaller scales contribute to a larger extent to the total summer and heavy rainfall, highlighting these as an important component of the regional water cycle. Figure 11 shows the TCS contributions to total summer and heavy rainfall between June and August, when most of TCSs are detected (Fig. 6). As for the MCSs, the largest contributions

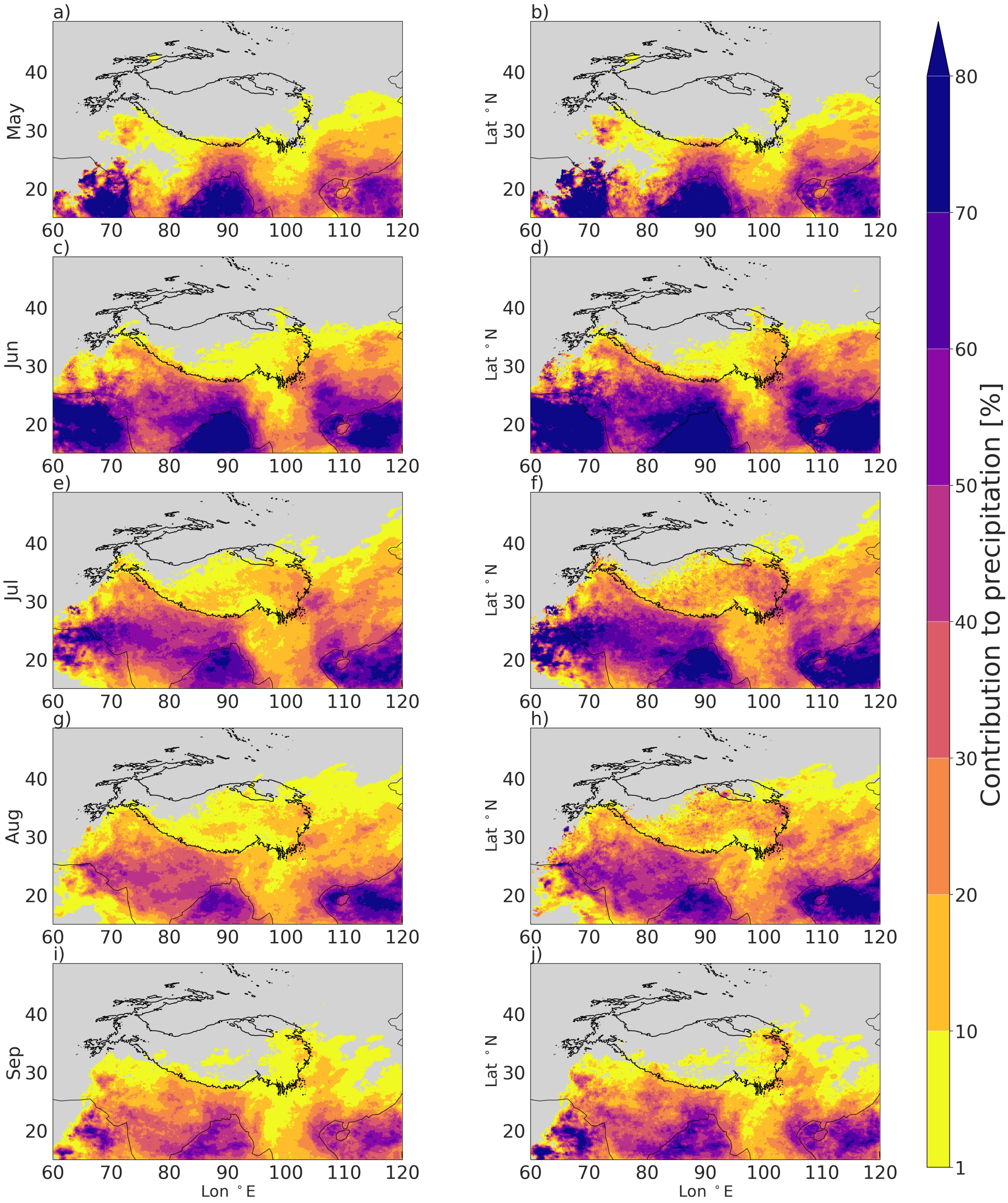

Figure 10. Maps of the monthly contribution of precipitation from MCSs, in % of total precipitation (a,c,e,g,i) and total heavy precipitation (b, d, f, h, j), which is the sum of precipitation produced by rain rates of at least 5 mm h^{-1} . The subplots show each month between May and September for the period 2000 to 2019.

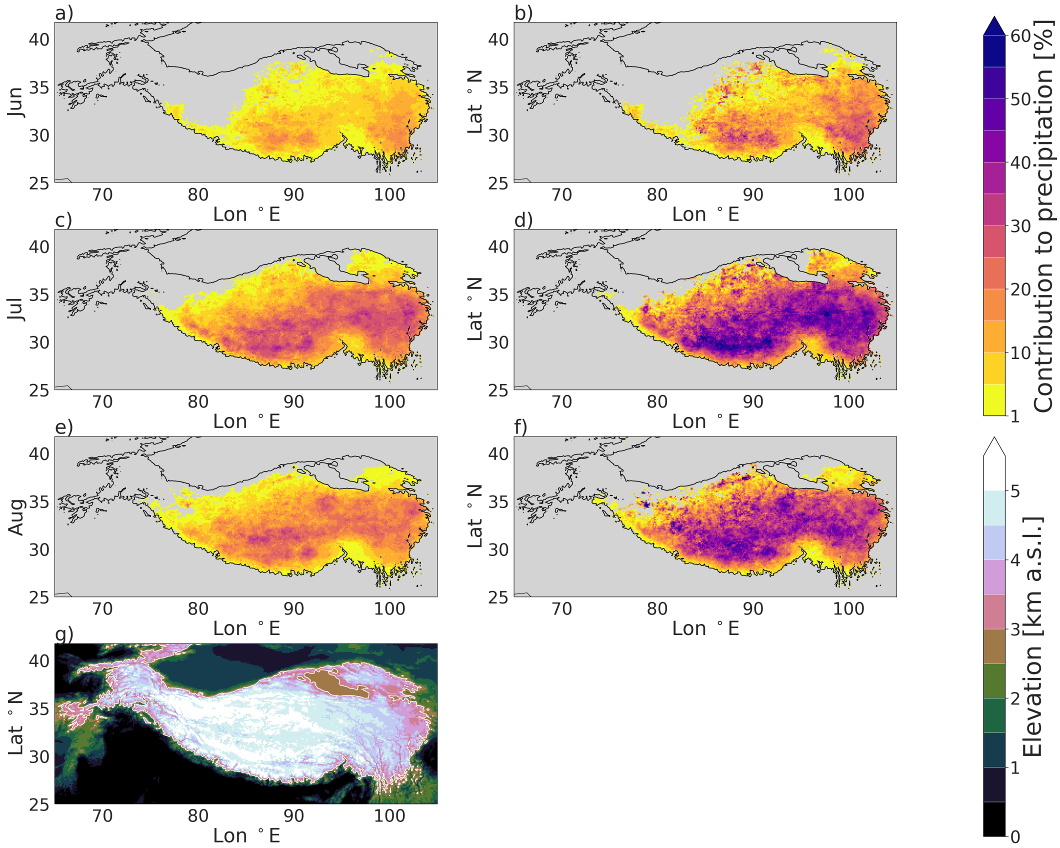

Figure 11. Same as in Figure 10, but for the smaller and more short-lived TCSs. These convective cells have approximately meso-β dimensions in the horizontal plane (20 to 200 km). Contributions are shown for June to August as the ratio of precipitation from TCSs to total precipitation (a,c,e) and to total heavy precipitation (b,d,f). The elevation of the TP [km a.s.l.] is also shown for context (g).

to rainfall occur in July and August, where TCSs account for between 25 and 50 % of the total precipitation over large areas of the central and eastern TP. Again, a strong difference between the contribution of these systems to total and heavy precipitation is visible. The contributions to heavy precipitation exhibit strong local maxima and therefore a patchy spatial pattern with many grid cells in the southern and eastern TP for which more than 60 % of local heavy precipitation is accounted for by tracked systems. A large area of high values for the contribution occurs at the eastern edge of the TP (Fig. 11). This region is the same region that had the highest values for MCS contributions over the TP (Fig. 10). There is no clear pattern linking the contribution to precipitation with topography, but it should be noted that small-scale convective systems contribute to summer precipitation even at elevations higher than 5,000 m a.s.l. (Fig. 11). This means that organisation of convection over a few 10s of km is not necessarily confined to the lower elevations over the eastern valleys of the TP.

3.3.2 Precipitation features

In the example snapshot in Figure 4, the convective core with heavy precipitation is surrounded by a larger area of stratiform precipitation with moderate rain rates and by an even larger area of non-precipitating clouds. Although stratiform cloud shields that develop alongside MCSs may extend over large areas, the convective part of a MCS produces large amounts of rainfall over short periods and is therefore of higher environmental and hydrological relevance than the stratiform part. Figure 12 summarises the key characteristics of precipitation features in the MCSs that are associated with rain rates > 5 mm h^{-1}, as an approximate differentiation for the more convective part of the MCS-induced rainfall. The precipitation features of MCSs in the TP + TPB are distinct from those in the LE region, because they have generally warmer cloud tops (Fig. 12a), less extreme rain rates (Fig. 12b) and smaller fractions of the total cloud area that is occupied by heavy precipitation (Fig. 12c).

As mentioned in Section 3.1, results from the different MCS tracking methods were similar, regardless of whether the T_b cold core or T_b heavy rain core criterion was applied (Table 2). This implies that MCS precipitation intensity is somewhat reflected in the observed mean brightness temperatures of the cloud features, because cloud cells that grow deeper during their lifetime have on average higher cloud tops (and hence colder brightness temperatures) and produce more intense precipitation. However, the relationship between brightness temperatures and precipitation intensification within a cloud is complex, and the pixels with the lowest temperatures do not usually correspond to the most convective part with heavy precipitation, but occur in the region where convection decays into cold stratiform clouds. Nevertheless, the general development of brightness temperatures during the MCS evolution is linked to precipitation intensity, so that the likelihood for extreme rainfall increases with colder cloud features (Klein et al., 2018). Therefore, the higher frequencies of low mean brightness temperatures and high rain rates in detected cloud features of the LE systems (Fig. 12a-b) suggest that MCSs that initiate and evolve over the plains are generally deeper and more intense systems than over the TP.

The distributions of the heavy rainfall area, expressed as a fraction of total cloud area, are right-skewed for all MCS types and show that for more than half of the identified MCSs, less than 25 % of the detected cloud area produces heavy precipitation (Fig. 12c). However, despite the small area such rain rates can produce substantial amounts of precipitation during short time periods, which is why the proportion of the total rainfall that is produced by higher rain rates shows a mirrored distribution for LE west and LE east. For the majority of these systems about 60 to 80 % of the total rainfall comes from heavy rain (Fig. 12d). This pattern is common for larger MCSs that have been found to produce around 40 % of stratiform and around 60 % of convective precipitation in other regions (Cheng et al., 1979; Rutledge et al., 1979). Indeed, for TP + TPB, the proportion of heavy rainfall instead exhibits a large range of values, which confirms again that most of the MCSs over and in the vicinity of the TP are not as well-developed as the MCSs in the downstream regions.

3.3.3 Heavy impact MCSs

The total rainfall amount produced by a MCS depends on the system's lifetime, size and intensity. The four MCS types presented in Figure 8 include MCSs with highly variable track characteristics. Thus, we further divide each MCS type into three categories, according to lifetime, size and intensity. To identify what characterises MCSs with a potentially heavy impact compared to MCSs that produce smaller amounts of precipitation, these MCS classes are examined with respect to the total amount of heavy precipitation they produce during their lifetime (Fig. 13). Figure 13 shows the distributions of total heavy precipitation (from rain rates $>$ 5mm h^{-1}) for the four MCS types divided into the three classes of lifetime, size and intensity.

The boxplot shows that the total amount of heavy precipitation varies substantially between the tracked MCSs. Differences between the total heavy precipitation distributions for the five previously defined MCS types (LE west, LE east, TP + TPB west, TP

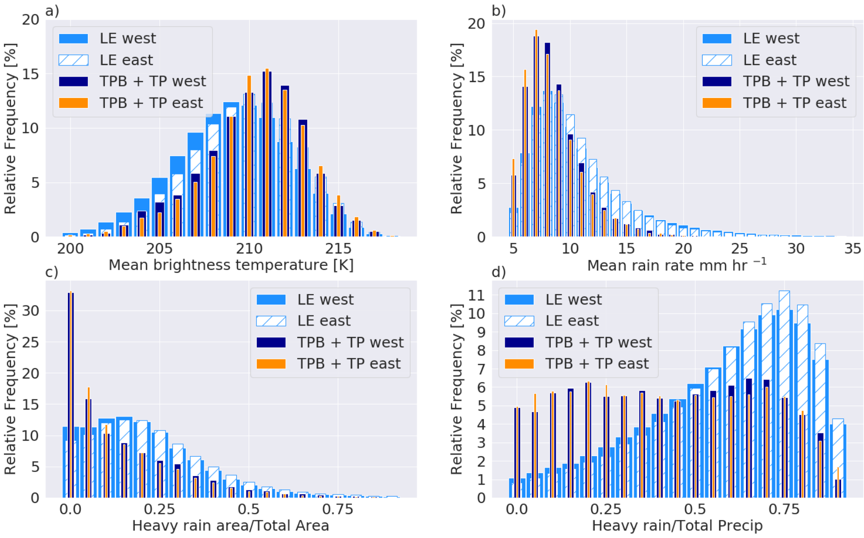

Figure 12. Characteristics of detected MCS cloud features that contain heavy rainfall (here defined as rainfall >5 mm h^{-1}). The histograms show the a) mean brightness temperatures [K], b) mean rain rate [mm h $^{-1}$], c) the proportion of the area with heavy rainfall in relation to the total cloud area and d) the amount of heavy rainfall in relation to total rainfall in the individual precipitating cloud features.

+ TPB east and TP) are mainly between LE and TP + TPB types, which supports our earlier finding that the genesis location (plains or mountains) is more important for the key characteristics and total amount of heavy precipitation than their respective propagation directions. Hence, both eastward- and westward-moving MCSs over lower and higher elevations may produce substantial amounts of heavy rainfall, but MCSs initiated over the TP or around its boundary are generally smaller and include less frequent extreme cases. Comparing lifetime, area and intensity for systems in the different categories, the most pronounced difference in total heavy rainfall is visible between systems that last longer than 24 hours and systems that are shorter-lived (Fig. 13a). The mean, maximum and outliers for the distributions of total heavy precipitation also increase as the area covered by the system increases (Fig. 13b). However, the effect of the area is stronger for LE systems than for TP + TPB (Fig. 13b). The total heavy precipitation is less obviously related to the temperature of the coldest (most convective) part of the system (Fig. 13c).

MCSs that are initiated over the TP are located in the lowest-precipitation range of the distribution for each category, which means that those systems produce the smallest amounts of heavy precipitation. This is related to the fact that the extreme categories with the highest lifetimes and largest extents only contain very few TP cases and that none of the TP cases had a cloud feature $<$ 200 K that extended over an area of 50,000 km^2. The MCS example case from July 2008 (Fig. 4) is also marked in Figure 13 (red cross). This MCS belongs to the TP + TPB east type and produced more heavy precipitation than most other TP + TPB systems. It falls into the largest category for mean extent, but produced less total heavy precipitation than LE systems in same extent category (Fig. 13a-b). The example MCS case also produced less total precipitation than most of the other TP + TPB east systems that persisted for more than 24 hours (Fig.

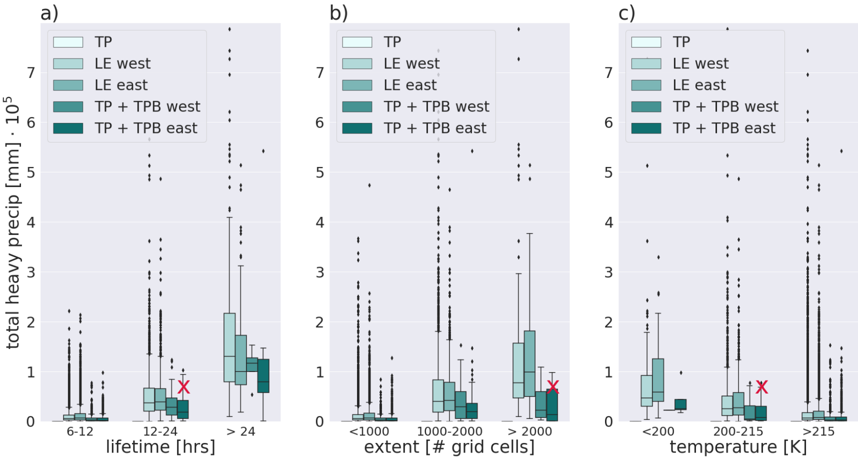

Figure 13. Boxplot showing the distribution of total heavy precipitation produced by eastward- and westward-moving MCSs which are initiated over the TP (TP), stay within or cross the TP (TP + TPB) and remain in the surrounding lower-elevation plains (LE). MCSs are divided into different classes depending on a) lifetime [hrs], b) extent [number of grid cells] and c) temperature [K]. The temperature refers to the lowest brightness temperature for a contiguous area within the cloud feature. The red cross highlights the MCS from of July 2008 used as a case study (see Section 2).

13a-b). This means that many detected MCS cases produce larger amounts of total heavy precipitation, which shows that MCSs with a similar potential impact occur frequently and pose a serious risk for the region they hit.

Figure 14 shows the joint frequency distributions for total heavy precipitation and maximum rain rate (a), minimum brightness temperature (b), system lifetime (c), and maximum area (c) of the MCSs that produce more than the 95th percentile of precipitation. This helps understanding the relationship between MCS characteristics and total heavy precipitation for heavy impact MCSs and shows, for instance, that the most intense rain rates or coldest brightness temperatures are not necessarily found in the systems that produce most heavy precipitation (Fig. 14a-b). Although none of the four characteristics stands out as a major controlling factor for the total heavy precipitation produced by the system, the joint frequencies show clearly that lifetime and maximum area have a greater effect than the intensity of rain rates or brightness temperatures. Hence, a MCS is more likely to produce large amounts of heavy precipitation the longer it persists and the larger it grows (Fig. 14c-d).

3.4 Large-scale atmospheric environments

The different characteristics between MCSs that interact with the topography of the TP compared to MCSs in the LE region are also reflected in the large-scale atmospheric environments that are associated with the respective MCS types. In Figures 15 to 18, we compare large-scale composites of the tracked MCSs, composed as as the 6-hour mean prior to their initiation stages. To describe the large-scale atmospheric conditions, we use mid-/upper-level wind circulation, atmospheric moisture transport and convective available potential energy (CAPE) taken from the ERA5 reanalysis (Hersbach et al., 2020). The composites are shown as anomalies which were computed by subtract-

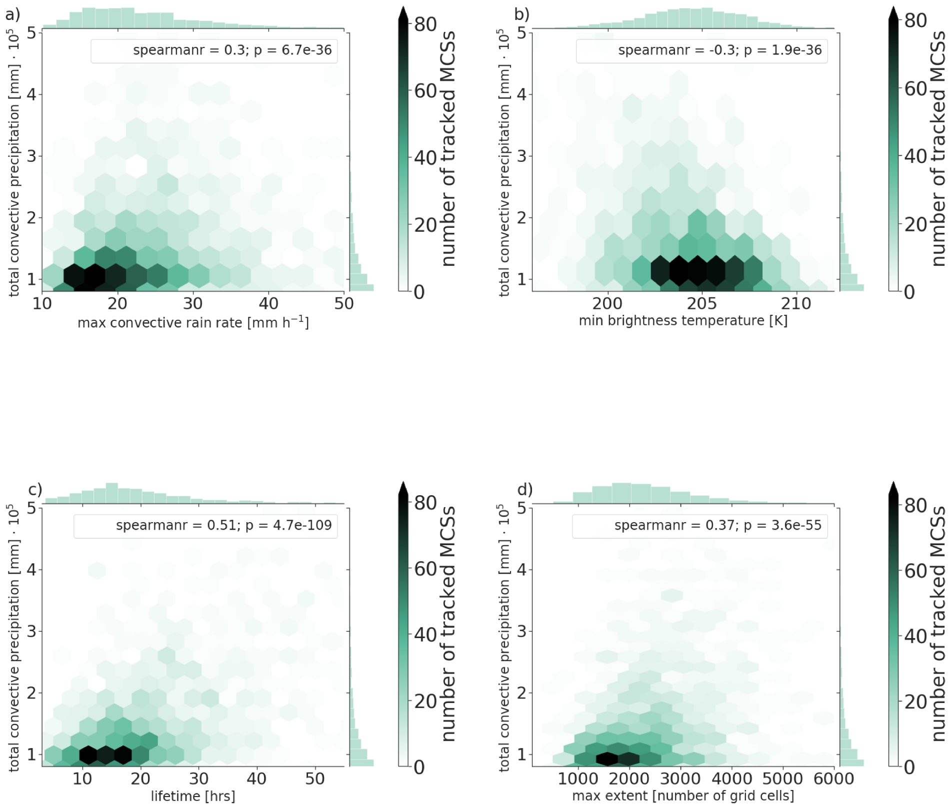

Figure 14. Joint frequency distributions for total heavy precipitation and a) maximum rain rate > 5 mm h^{-1}, b) minimum brightness temperature [K], c) lifetime [hrs] and d) maximum area of precipitation > 5 mm h^{-1} [number of grid cells] for the MCS that produce more than the 95th percentile of total integrated rainfall from rain rates above 5 mm h^{-1}. The colour scale indicates the number of identified MCS tracks which correspond to the values shown in the joint space. The histograms on the x and y axes show the individual frequencies of each variable.

ing the summer climatology 2000 to 2019 (displayed in the lower panels) from the composite mean. Positive anomalies indicate hence that the respective variable exhibits higher values for the MCS composite compared to the summer mean. We focus on the six hours prior to the first MCS detection, in order to examine synoptic patterns which may favour the initiation at a stage where no feedback of the MCSs to the large-scale environment has been introduced yet. Given the large number of MCSs with different intensities during the past two decades, the composite analysis focuses on MCSs that belong to the 95^{th} percentile for values of total MCS-induced precipitation (as in Fig. 14). Bearing in mind that various large-scale circulation processes may favour the initiation of convection in the diversified downstream regions, two major regions of MCS initiation in the LE are inspected (Fig. 7): over the Bay of Bengal (BOB) and over China.

We look at the upper-level dynamic forcing which is particularly important for the TP, where most locations have surface pressures close to 500 hPa. The 200 hPa zonal wind serves as a proxy for the strength and location of the subtropical westerly jet (Schiemann et al., 2009), which in turn is influenced by the anticyclonic circulation around the South Asian High (with large parts of its main body located over the Iranian and Tibetan Plateau). Previous studies have shown that intense rainfall events over South-East Asia are often linked to anomalous water vapor transport and upper-level circulation caused by subseasonal variations of the South Asian High movement and intensity (Jia & Yang, 2013; Ren et al., 2015; Shang et al., 2019). In addition, we look at the 500 hPa geopotential, as an indicator for horizontal pressure gradients over the South-East Asian continent and low-level circulation over the TP.

A prominent large-scale feature for MCSs that are initiated over the TP and TCSs is the intensification of the westerly jet, which is visible through the positive anomaly in the 200 hPa zonal wind over the northern TP and the simultaneous negative anomaly south of the major jet axis (Fig. 15a-b), which is located around 40°N in the climatology (Fig. 15f). Schiemann et al. (2009) have highlighted that the intensification and northward shift of the westerlies from June onward are associated with a strong Indian summer monsoon circulation and hence increased moisture supply and diabatic heating over the TP. Moreover, Li et al. (2014) found that the westerly jet can favour cyclonic rotation south of its maximum speed through upper-level divergence and convergence close to the surface over the TP. The anticyclonic circulation of the South Asian High is manifested through the positive anomalies in upper-level zonal winds and shows also a prominent intensification for TP and TCS (Fig. 15 a-b). This is consistent with Lai et al. (2021), who showed that the South Asian High played a crucial role in controlling the seasonality of TP precipitation in anomalously wet years. TPB, LE BOB and LE China show the inverse pattern with a weaker anticyclonic circulation (Fig. 15c-e).

The strong positive upper-level zonal winds south of the TP and the southerly shift of the westerly jets for MCSs over China (Fig. 15e) are accompanied by an intensified horizontal pressure gradient at 500 hPa (Fig. 16e). Similar to LE BOB (Fig. 16c), but in contrast to TP and TCS (Fig. 16a-b), LE China shows a strong decrease in geopotential northeast of the TP, which suggests a strong upper-level wind forcing due to the enhanced north-south gradient in pressure (Fig. 15e).

All MCS types are clearly connected to anomalies in atmospheric water vapor transport to the respective regions of MCS genesis (Fig. 17a-e). It is noticeable that the moisture transport from the Bay of Bengal towards the mountain regions is enhanced for TP and TCS (Fig. 17a-b) and that the main region of this positive atmospheric water vapor transport south of the Himalayas exhibits in contrast negative anomalies for TPB, LE BOB and LE China (Fig. 17c-e). Whereas the Southern ocean is the key moisture source for TP, TCS and LE BOB, TPB and LE China are associated with negative anomalies over the Arabian Sea and Bay of Bengal (Fig. 17c,e). This suggests that most of the moisture for MCSs that are initiated over China comes from the continent and from the South China Sea.

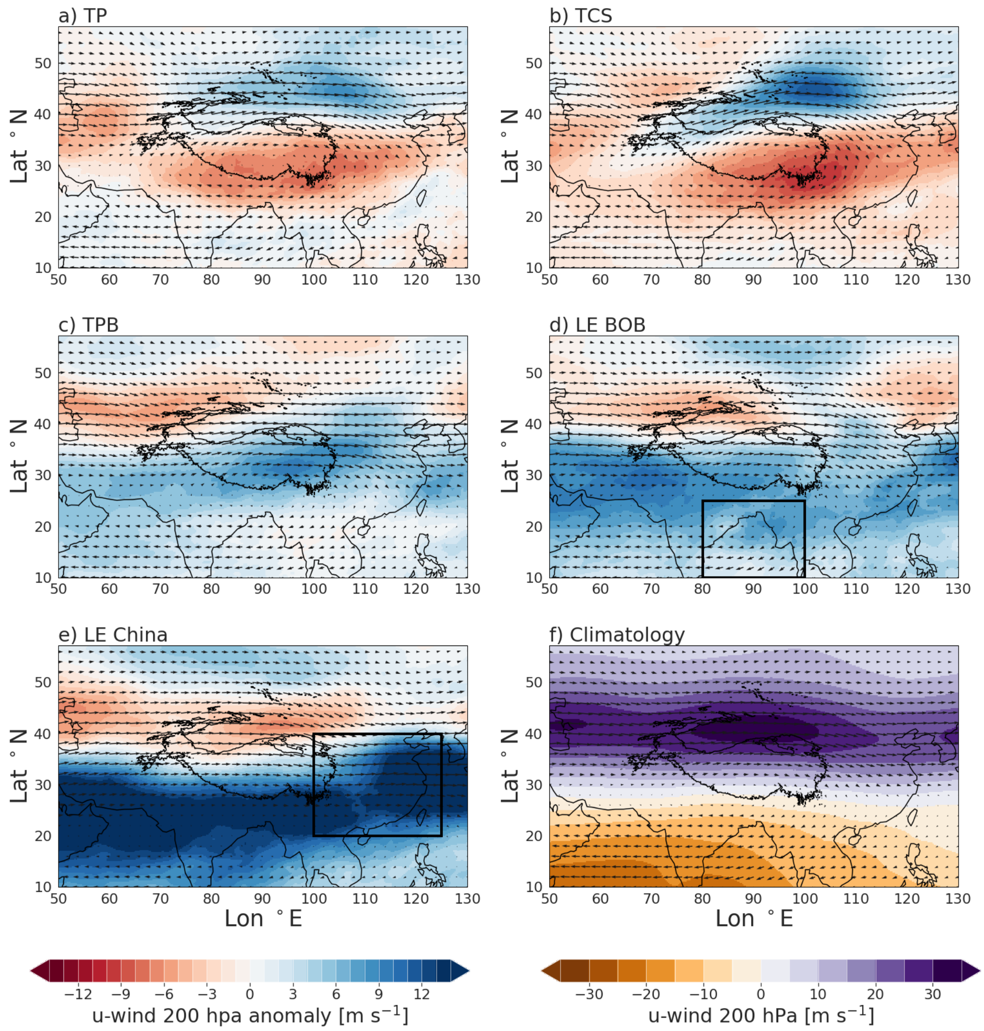

Figure 15. ERA5 composite maps for 200 hPa wind circulation composed as the mean of six hourly time steps prior to the initiation stages of different MCS types: a) TCS, b) TP, c) TPB, d) LE BOB and e) LE China. The shading shows the anomaly of the zonal wind component at 200 hPa, computed as the composite mean minus the climatology for June to August for the period 2000 to 2019 (shown in panel f).

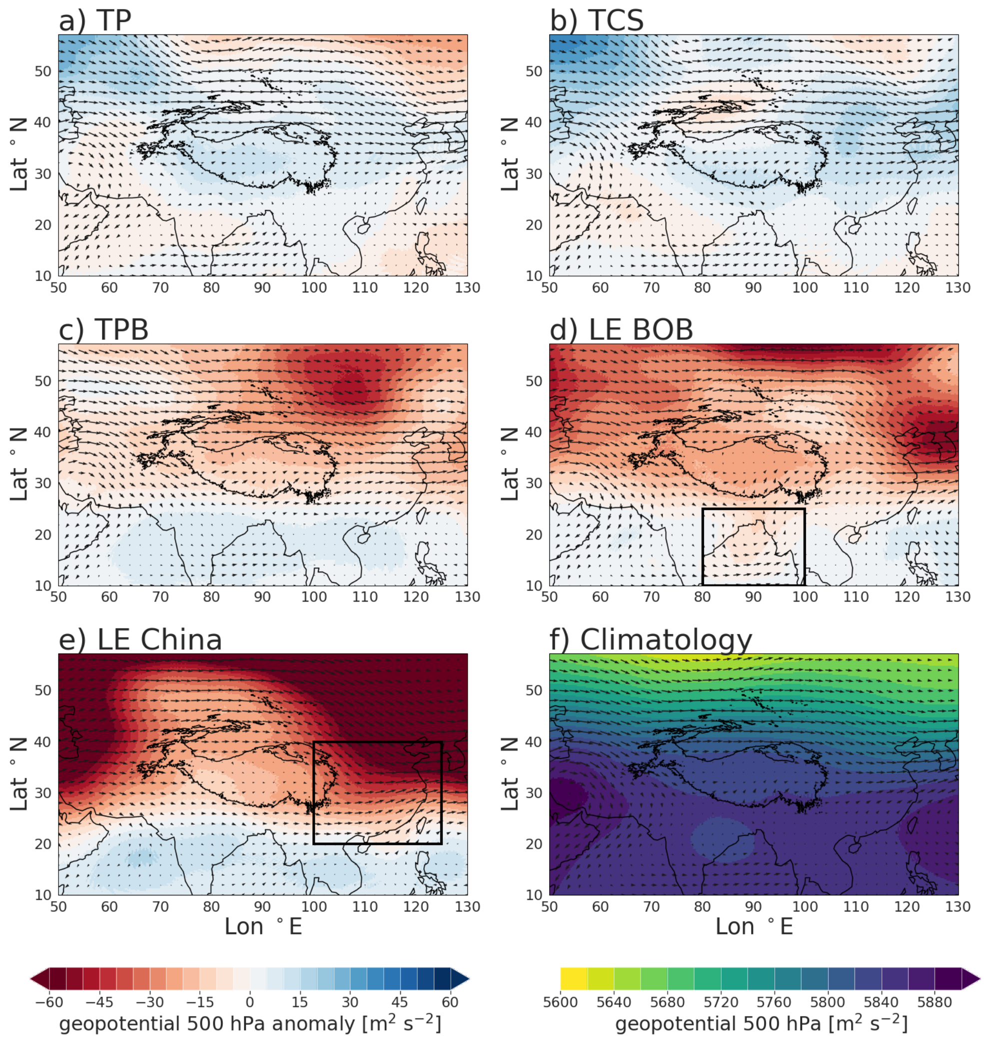

Figure 16. Same as in Figure 15, but for 500 hPa wind circulation. The shading indicates shows the anomaly of the 500 hPa geopotential height.

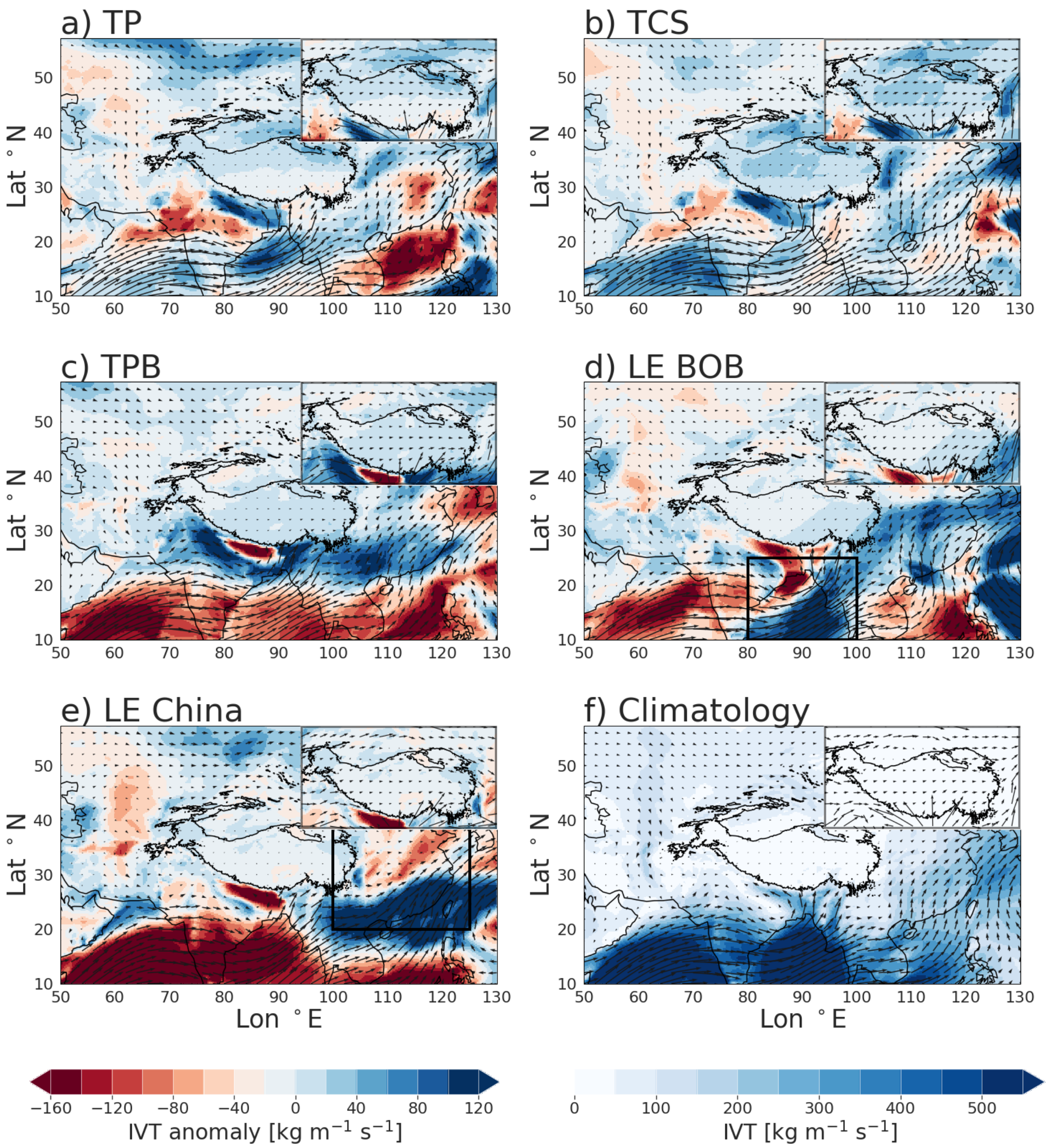

Figure 17. Same as in Figure 15, but for vertically integrated water vapour transport. The arrows are the vectors of the vertically integrated water vapour fluxes (qu and qv) and the shading is the anomaly in total vertically integrated water vapour transport (IVT), defined as $\sqrt{qu^2 + qv^2}$. The top right figure is a zoomed in image of the TP using a multiplying factor of 1.5 to show more clearly from which direction the water vapour advects.

In addition to the large-scale wind forcing and sufficient moisture supply, a key factor for organised convection is atmospheric instability, which is indicated by CAPE (Fig. 18). Figure 18a shows a strong positive anomaly in CAPE over the TP and in the downstream regions east of the TP (over Mainland China), when MCSs are initiated over the TP. The same is true for TCSs, where the positive CAPE anomaly over the central TP is even stronger (Fig. 18b). The accumulation of CAPE appears as an important factor for convection initiation over and close to the mountains, because these regions exhibit on average CAPE values below 400 J kg^{-1} (Fig. 18e), which is not sufficient to develop severe storms (Kirkpatrick et al., 2011). Furthermore, the positive CAPE anomalies over the TP and in the downstream regions to the east occur simultaneously with a strong negative CAPE anomaly at the Indian east coast (Fig. 18a-b). TPB systems do not show the same positive anomaly over the TP, but instead positive anomalies over the ocean and the South Asia (Fig. 18c). The bimodal ocean-land pattern that was visible for TP and TCS is the inverse for LE BOB, where a strong negative CAPE anomaly over Mainland China occurs simultaneously with a strong positive CAPE anomaly over the MCS genesis region, the Bay of Bengal (Fig. 18d). The fact that the average conditions during summer exhibit large amounts of CAPE (> 1800 J kg^{-1}) over the ocean (Fig. 18e) shows that the accumulation of CAPE is a particularly important factor for MCSs over and east of the TP, because a stronger dynamical and thermodynamical forcing is needed for convective storms to develop. Given that the high MCS frequency over the Bay of Bengal and Indian subcontinent (Fig. 7), this means that convection can more frequently develop in these regions even with weaker dynamical and thermodynamical disturbances. Other hotspot regions for convective storms also show that environments with high average CAPE values require smaller anomalies for storms to develop, for instance the U.S. Great Plains where CAPE anomalies are substantially smaller during summer compared to spring (Song et al., 2019).

The fact that MCS initiation over the TP (TP and TCS) is related to enhanced moisture transport, a more intense upper-level jet and anticyclonic circulation as well as strong positive CAPE suggests that stronger dynamic and thermodynamic perturbations are needed to initiate larger MCSs over on the leeside of the mountains. The positive CAPE anomaly to the east of the TP also shows that the synoptic conditions favouring MCS initiation over the TP could potentially lead to extreme events when the accumulated CAPE in the eastern downstream regions is released.

4 Discussion

4.1 Role of MCSs in precipitation

Previous studies have highlighted MCSs as the main source of summer precipitation over the TP. Here, we argue that it is important to take the scale of convection into account, when drawing conclusions about as MCSs as a component of the regional water cycle of the TP. Our results show that larger MCSs are a main component in the water cycle in the LE region, whereas small-scale convection is a more important source of precipitation over the TP. The reasons for discrepancies in total MCS numbers and MCS-associated precipitation between previous studies and our findings is three-fold. Firstly, our method for MCS tracking is less likely to include cirrus clouds or cold surfaces because we assure that cloud cold tops are also associated with a heavy rain core. Secondly, our method for calculating MCS-associated precipitation differs from commonly used methods. Many studies use a radius approach, where all precipitation within a certain radius of the MCS centre is considered to be MCS-induced precipitation, instead of tracking precipitation features within cloud cells as we have done here. Our results show that the area with heavy precipitation of some MCSs can vary significantly (Fig. 12), and the method we have developed here could therefore give a more accurate estimate of precipitation associated with a MCS, which is most likely dependent on the size of the MCS. Additionally, our calculated MCS contributions to precipitation are consistent with those es-

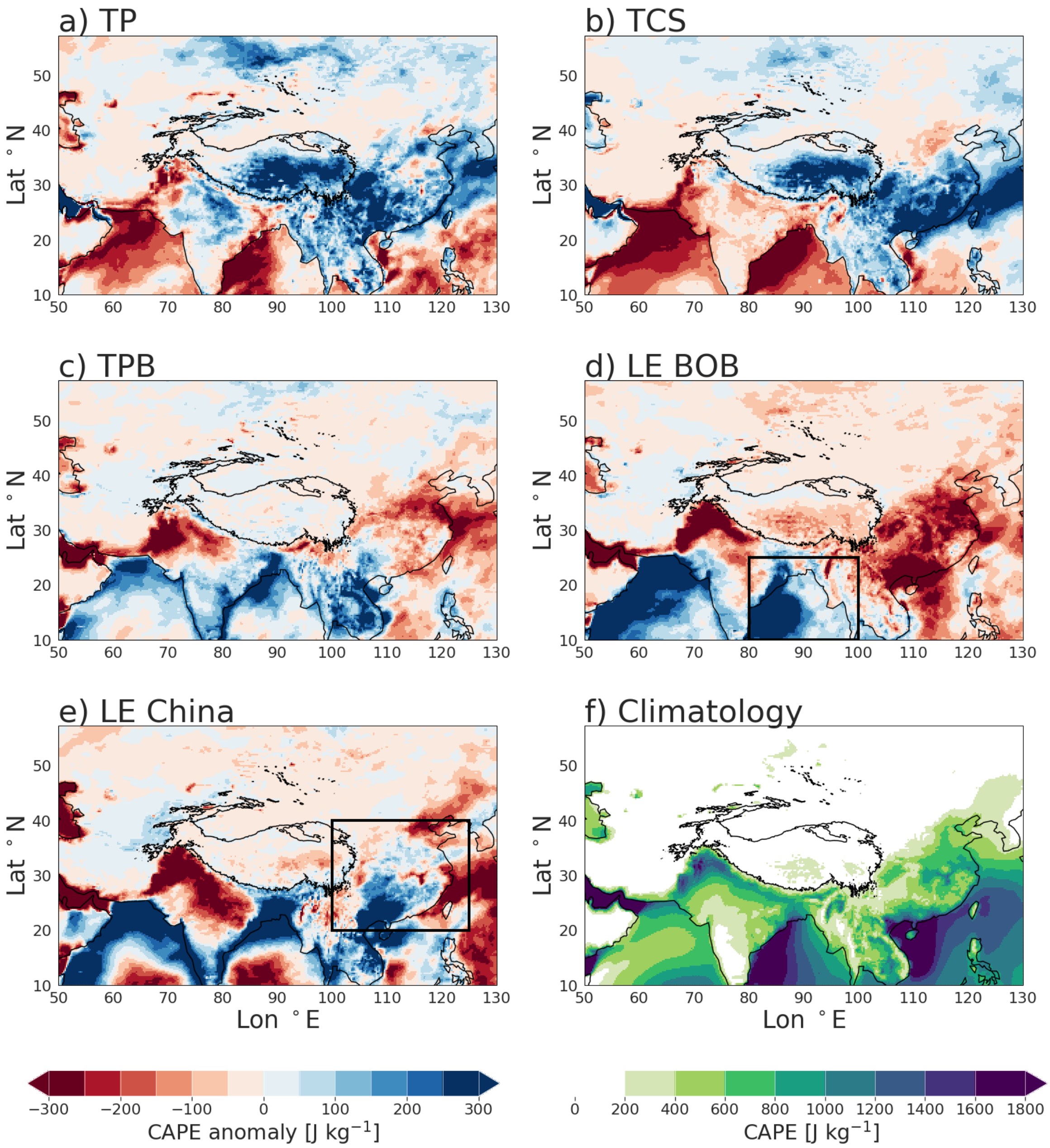

Figure 18. Same as in Figure 15, but for the anomalies in convective available potential energy (CAPE).

timated by Feng et al. (2021), who use a similar method for MCS tracking and precipitation attribution. Thirdly, we demonstrated that the number of tracked MCSs over the higher altitudes is very sensitive to the area threshold and that meso-β convective systems have higher contributions to total summer and heavy precipitation over the TP than meso-α systems (with similar dimensions as MCC (Maddox, 1980)).

The MCS contributions to heavy precipitation (Fig. 10b, d, f, h, j; Fig. 11b, d, f) revealed that there is heavy precipitation over the TP that could not be associated with the tracked cloud clusters. This suggests that convective modes that are not targeted by our tracking algorithm, such as isolated thunderstorms and deep convection, also play a significant role for summer precipitation. A similar conclusion was drawn by Houze et al. (2007) who investigated deep convective features based on Tropical Rainfall Measuring Mission (TRMM) Precipitation Radar (PR) data and found that deep convective echoes occur over the TP in a scattered manner, whereas more prominent mesoscale convective features organised along the Himalayan ranges. Possible explanations for the dominance of isolated convective cells instead of organised convection could be the highly varying topography that act as mechanical barriers, limited moisture supply and cirrus clouds, which may locally inhibit convective heating over some parts during summer (Roebber et al., 2002). The simultaneous occurrence of cirrus clouds and convective clouds, as revealed in the bimodal cloud top height distribution over the TP during summer (Chen et al., 2018; Kukulies et al., 2019), suggests that the effect of cirrus clouds is not negligible.

According to the definition used here, MCSs with meso-α dimensions were occasionally found over the TP (in total 1237 cases over 20 years). These are associated with heavy precipitation between late afternoon and early evening (Fig. 9a) and have the highest contributions to heavy precipitation in the eastern parts of the TP (Fig. 10d,f,h). Albeit the total amount of heavy precipitation produced by these MCSs was relatively small compared to that from MCSs over the Indo-Gangetic Plain and along the Indian coast (due to generally lower intensity and lifetimes). However, these MCSs can still be very destructive, in particular when they do not move far and produce instead a lot of rainfall over the same populated area, like in the case that was shown in Section 3.1 that lead to severe flooding in the Sichuan basin (Feng et al., 2014). Because such MCSs are particularly hazardous, future projections for both MCS frequency, intensity, and also their likelihood to occur as quasi-stationary or back-building types are needed.

The importance of MCSs for summer mean and heavy rainfall was significantly higher in most of the LE region south of the Himalayas than over the TP. Densely populated regions south of the Himalayas and in the Indo-Gangetic Plain experience frequent MCS events, which produce substantial rainfall amounts due to their longevity and large size. Feng et al. (2018) found that long-lived MCSs over the Great Plains in the USA produced 2–3 times more precipitation than short-lived MCSs. A similar result was found in this study, where both mean and maximum total heavy precipitation of MCSs that persisted longer than 24 hours were about twice as high as MCSs that persisted between 12 and 24 hours and four times higher than MCSs that persisted for up to 12 hours. The fact that the differences in MCS contributions to total vs. total heavy precipitation were relatively small in the LE region, shows that MCSs in the LE region are not only an important factor for local extremes, but also a significant component in the water cycle. Hence, changes in MCS patterns do not only affect the risk of severe weather for populated regions, but can also lead to changes in the accumulated rainfall during one season and thereby affect crop yields and water resources.

It should be noted that the contribution of MCSs to precipitation may have been underestimated in the downstream regions, because our MCS tracking method was optimised for the TP. Since cloud top temperatures for deep convective cells of the same depth are higher over lower-elevation regions than the TP, an improvement of MCS tracking for these regions could be achieved by considering the difference of cloud top temperatures to local surface temperatures rather than applying one brightness temperature threshold over different altitudes. Additionally, the used data product GPM IMERG may underestimate very high rain rates, which will be discussed in more detail in the next section.

4.2 Retrieval uncertainties

The results of this paper suggest that the role of MCSs in precipitation can be illuminated by utilising high-resolution precipitation datasets like the newly available GPM IMERG v06 in combination with IR imagery from geostationary satellites. This is a way to reduce uncertainties related to IR brightness temperatures, especially if the region of interest includes various surface types and complex topography. Nonetheless, one should also be aware of the uncertainties related to satellite precipitation retrievals, particularly over high terrain.

Three specific aspects of uncertainty are related to snowfall detection, the underestimation of warm orographic rain and the underestimation of intense convective precipitation. It has repeatedly been shown that the inclusion of Dual-Frequency Precipitation Radar (DPR) in GPM IMERG exhibits improved capabilities for snowfall detection both over the TP (Ma et al., 2016) and in other mountain regions (Wen et al., 2016). Spaceborne radar observations can significantly improve rain retrievals from IR and microwave observations, because the active radar sensors can more accurately derive the precipitation phase. Additionally, radar reflectivity is more directly linked to surface precipitation intensity than passive microwave observations, which infer rain rates based on ice scattering aloft. However, radar sensors such as DPR have a lower spatial coverage and over snow surfaces, the input data for the IMERG retrieval are only obtained from passive microwave sensors. This can lead to erroneous snowfall estimations and to wet biases due to falsely detected precipitation events as a consequence of increased scattering at the surface. At the same time, warm orographic precipitation may be underestimated in regions with highly complex topography, because of low IR brightness temperature signatures and absent ice scattering, which is crucial for precipitation detection by passive satellite sensors. The GPM IMERG retrieval may also underestimate very intense hourly rain rates. In a comparison between IMERG and a ground-radar network over the US, it has, for instance, been shown that the occurrence frequencies of convective rainfall in MCSs (here defined as > 10 mm h^{-1}) were significantly underestimated by IMERG in all seasons with the strongest bias during the summer season (Cui et al., 2020). This is also true for smaller isolated cells of deep convection, because the spatial averaging of reflectivities at the resolution of the precipitation radar can lead to a significant underestimation of the rain rates in such systems (Duan et al., 2015).

An additional point is that sensor- and retrieval-related biases can only to a very limited extent be corrected by gauge calibration, because meteorological stations in the TP region are sparsely distributed and mainly located in the valleys. Even though it has been shown that GPM IMERG reduces the well-known wet bias of total and seasonal mean precipitation over the TP (Xu et al., 2017; Zhang et al., 2018), the uncertainties in subhourly and hourly precipitation have not been sufficiently studied. The evaluation of satellite precipitation estimates against in-situ observations is necessary to better understand various biases that can occur in high and complex terrains and this has not extensively been done over the TP. Systematic validation studies such as Cui et al., (2020) are therefore needed to quantify the effect of various biases on MCS feature detection and tracking before MCS datasets can be used for hydrological applications.

Given the above-named uncertainties, the absolute values of retrieved rain rates should be interpreted with caution, because especially the higher rain rates (e.g. > 5mm h^{-1}) and consequently the total accumulated precipitation of one MCS may be underestimated in this study. Nevertheless, GPM IMERG provides robust information whether or not contiguous areas of relatively higher rain rates are present. Therefore, we think that it is a useful dataset to examine the main features of precipitation within MCSs in a comparative way. To get a more complete understanding of different convective modes and their precipitation features over the TP, further studies should also consider the vertical structure of the organised convective cells.

4.3 Possible mechanisms for MCS formation

This study provides an observational perspective on MCSs over a larger region, where multiple processes may lead to the organisation of convection at the mesoscale. Most of the MCSs in the LE region over land were found south of the TP, over the Indo-Gangetic Plain and close to the Himalayas, as well as over the southern Indian subcontinent and at the coast of the Bay of Bengal. Both land and ocean south of the TP are influenced by frequent monsoon low pressure systems during the wet season, and these have been associated with barotropic instabilities that may be amplified by wind-moisture feedbacks (Boos et al., 2017; Diaz & Boos, 2019). Because we do not explicitly exclude tropical cyclones and monsoon low pressure systems, the high track densities over the Indian subcontinent and ocean (Fig. 7) may contain such systems, even though the driving mechanisms are different from those of MCSs.

The mechanisms for organisation of convection over and close to the TP are most likely very different from MCS formation over the plains, because of the influence of mountain barriers, local wind systems and the orographically modified large-scale circulation. The distinct diurnal evolution of MCSs that are initiated over the TP (Fig. 9) and the large contributions of small-scale convective cells (TCSs) to precipitation (Fig. 11) emphasise the importance of local conditions and topography. The dominating pattern for MCS initiation over the TP in the afternoon hours compared to the diversified patterns in the surroundings (Fig. 9) is consistent with Zheng et al. (2008), who found that single-peak MCSs are more common over mountains and plateaus whereas multi-peak MCSs are more common over basins and plains. This means that convection over the TP is closely related to the diurnal flow patterns and surface heating, whereas MCSs in the TPB region and over the ocean do not occur at a specific time of the day. In the same study, the authors concluded that multi-peak MCSs also correspond to longer-lived MCSs and MCSs with larger horizontal dimensions. This is also consistent with our findings, as the second peak in the initiation times for all MCSs (Fig. 8b) can be mainly attributed to LE systems that are more long-lived, larger and generally more intense than MCS over the TP (Fig. 14).

An important trigger mechanism for organised convection over and close to the mountains could be frequently occurring are mesoscale disturbances in vorticity around 500 hPa, namely Tibetan Plateau vortices (TPVs) (Feng et al., 2017; Hunt et al., 2018; Curio et al., 2019). While the presence and strength of TPVs is not clearly distinguishable in the mean geopotential field at 5,000 hPa for MCS composites over the TP (Fig. 16a-b), this study shows that MCSs that are initiated over the TP are clearly associated with positive anomalies of the upper-level westerly jet. This large-scale feature is most likely also linked to the occurrence frequency and intensity of TPVs, as Curio et al. (2019) showed that the position and strength of the westerly jet controls the travel distance of TPVs. The TP is usually marked by limited moisture supply and CAPE (Fig. 18a-b), which show strong positive anomalies when MCSs are initiated over the high altitudes. This means that the intensified westerly jet may create favourable conditions for enhanced moisture supply and dynamic/thermodynamic disturbances, such as TPVs. Furthermore, it has been suggested in many studies that TPVs are important precipitation-bearing systems for the TP. For instance, Curio et al. (2019) demonstrated that a significant part of the plateau-scale precipitation occurs within a 3° radius of tracked TPV centres. The results from this study suggest, however, that the precipitation and cloud features identifiable in satellite observations occur at smaller scales and less frequently over high altitudes than TPVs. This suggests that the relationship between mesoscale disturbances in vorticity and organisation of convection is more complex than assuming that TPVs always result in well-developed MCSs. Future studies on the linkages between TPVs and observed MCS features as well as isolated deep convection, could provide valuable insights into mesoscale dynamics over the TP, as TPVs may also affect the water vapor transport to and from the TP.

The systems that made the greatest contributions to precipitation >5 mm h^{-1} over the TP (including both MCSs and TCSs) were located in the eastern part of the TP. This regional pattern may be related to surface properties, such as soil moisture and vegetation, which can regulate heat fluxes in the boundary layer (Talib et al., 2021) and thereby increase the convective instability at higher altitudes. This has, for instance, been suggested by Sugimoto and Ueno (2012) who found that soil moisture played a crucial role for convection initiation over the eastern TP. Barton et al. (2021) found that regions with higher soil moisture favour strong convection over the TP, but that vegetation, topography and background winds are additional factors that affect this relationship. Outside of the monsoon season, only very few systems have been detected. The few cloud clusters with a heavy rain core during the cold season are therefore probably driven by other mechanisms than organisation of convection, such as the lake-effect, which has been shown to trigger severe snow storms over the TP (Dai et al., 2020).

The complex patterns of MCSs at different spatial scales and highly varying precipitation features summarised in this study suggest that convection-permitting simulations are needed to provide a more complete picture of the underlying dynamics for precipitation formation in the TP region. In other regions, such as North America, it has been shown that convection-permitting simulations realistically capture the main characteristics of MCSs and associated precipitation (Prein et al., 2017). Such simulations could hence be a promising tool to understand the essential ingredients for mountain convection to organize into larger systems. So far, there are no studies that have looked at MCSs over the TP and in the TP downstream regions using model simulations with spatial resolutions finer than 30 km, although a few simulations with finer resolutions exist (Ou et al., 2020; Zhou et al., 2021). The existing and future fine resolution modelling over the TP should be used to explore the dynamics of the MCSs, in order to effectively represent small convective features in the TP downstream region, particularly those which are close to the 3,000 m boundary and interact with the topography.

5 Summary and conclusions

This study provides an observational perspective of MCSs in the TP region and elucidates the role of MCSs in seasonal and heavy precipitation. We tracked MCSs by co-locating brightness temperatures from IR satellite imagery and precipitation estimates from GPM IMERG for the period 2000 – 2019. Spatial and temporal characteristics of MCS tracks, their associated precipitation features and large-scale atmospheric environments were examined over the TP, around the TPB and in the LE region.

By comparing four different tracking methods, we have shown that it is useful to apply additional criteria that assure the development of deep convection and heavy precipitation, when IR brightness temperature thresholds are used to track MCSs in satellite imagery. To be considered a MCS in this study, cloud features (defined as a region $\leq$ 221 K over 50,000 km^2) had to persist for at least 3 hours. In addition, the connected cloud features had to contain a region with brightness temperatures below 200 K and a region with rain rates $\geq$ 5 mm h^{-1} that extends over at least 10 % of the minimum cloud area. These extra criteria significantly reduced the number of falsely identified MCSs as a consequence of the presence of cirrus clouds or cold surfaces in high mountain regions and results in a more realistic seasonal cycle for MCS frequency with a distinct summer peak. Most of the cases which showed a drop in brightness temperature < 200 K also contained a core with heavy rain and consequently the number of classified MCS tracks reduced only slightly for T_b *heavy rain core* compared to T_b *cold core*. These two criteria also resulted in the same key statistics, which means that they can be used interchangeably, but the use of both precipitation and brightness temperature data remains advantageous because it allows precipitation features to be identified and examined in the tracked clouds cells.

Most of the MCSs identified using our tracking method were found over the Indian subcontinent and Bay of Bengal. Over the oceans, MCS contributed to more than 80 % of the total precipitation during the onset of the Indian summer monsoon (May-June). Regions over land, where MCSs account for more than 50 % of the total precipitation between July and August were the Indo-Gangetic Plain, the southern foothills of the Himalayan mountain range as well as the Sichuan and Yangtze river basins. Our results showed also that MCSs with the highest amounts of total heavy precipitation were characterised by longevity and large cloud extents rather than by high intensities.

MCSs over the TP and at the TPB were generally less frequent compared to the LE region. We detected substantial differences in the diurnal evolution, longevity, precipitation features and large-scale atmospheric environments between MCSs that interact with the mountains (TPB + TP) and MCSs in the LE region. One notable characteristic of the large-scale environments that was associated with MCS initiation over the TP was, for instance, the intensification of the anticyclonic circulation around the South Asin High accompanied with positive water vapor transport along the Himalayas and increased CAPE over the TP and China. Furthermore, we have shown that the contribution of MCS-induced precipitation to the total summer precipitation (total heavy precipitation) over most parts of the TP corresponded to 10 - 20% (20 - 50%) in July, but below 10 % (30 %) during the other monsoon months. Even though the MCS contribution to total heavy summer precipitation over the TP was significantly higher than the MCS contribution to total summer precipitation, it was still significantly lower than in most of the LE region. This is consistent with our result that MCSs over the TP were generally less frequent, smaller and more short-lived, and can most likely be attributed to the limited moisture supply over the mountains. Convective systems at the meso-β-scale showed higher contributions to the total and heavy precipitation over the TP during summer than the larger MCSs. This finding highlights the significance of more localised precipitation systems and convective modes for the water cycle over the TP, in contrast to large convective clusters which occur mainly in the downstream regions south and east of the TP. Model simulations at convective scales may have the potential to improve the understanding of mesoscale dynamics for precipitation formation over the TP.

Acknowledgments

We thank three anonymous reviewers for their constructive comments and suggestions. The study was supported by the Swedish National Space Agency (SNSA: 188/18 4) and the Chinese Academy of Sciences (XDA2006040103). It is a contribution no 7 to CORDEX-FPS-CPTP and Swedish MERGE. We thank the providers of key datasets used here (NASA, NCEP). NCEP/CPC Brightness temperatures can be downloaded from `https://disc.gsfc.nasa.gov/datasets/GPM_MERGIR_V1/summary` and GPM IMERG v06 can be downloaded from `https://disc.gsfc.nasa.gov/datasets/GPM_3IMERGHH_06/summary` or from `https://gpm.nasa.gov/data/directory`. The latest version of the hourly ERA5 reanalysis at pressure levels can be accessed through Copernicus Climate Data Store: `https://cds.climate.copernicus.eu/cdsapp#!/dataset/reanalysis-era5-pressure-levels?tab=overview`.

The MCS dataset can be downloaded in form of annual files at `https://doi.org/10.5281/zenodo.4767152`.

The code for the MCS tracking algorithm can be found at `https://github.com/JuliaKukulies/mcs_tracking/tree/master/CTT/tracking`.

References

Ban, N., Schmidli, J., & Schär, C. (2015). Heavy precipitation in a changing climate: Does short-term summer precipitation increase faster? *Geophysical Research Letters*, *42*(4), 1165–1172.

Barton, E., Taylor, C., Klein, C., Harris, P., & Meng, X. (2021). Observed soil moisture impact on strong convection over mountainous tibetan plateau. *Journal of Hydrometeorology*, *22*(3), 561–572.

Berg, P., Moseley, C., & Haerter, J. O. (2013). Strong increase in convective precipitation in response to higher temperatures. *Nature Geoscience*, *6*(3), 181–185.

Bibi, S., Wang, L., Li, X., Zhou, J., Chen, D., & Yao, T. (2018). Climatic and associated cryospheric, biospheric, and hydrological changes on the tibetan plateau: a review. *International Journal of Climatology*, *38*, e1–e17.

Boos, W. R., Mapes, B. E., & Murthy, V. S. (2017). Potential vorticity structure and propagation mechanism of indian monsoon depressions. In *The global monsoon system: Research and forecast* (pp. 187–199). World Scientific.

Cheeks, S. M., Fueglistaler, S., & Garner, S. T. (2020). A satellite-based climatology of central and southeastern us mesoscale convective systems. *Monthly Weather Review*, *148*(6), 2607–2621.

Chen, D., Guo, J., Yao, D., Lin, Y., Zhao, C., Min, M., ... Chen, T. (2019). Mesoscale convective systems in the asian monsoon region from advanced himawari imager: Algorithms and preliminary results. *Journal of Geophysical Research: Atmospheres*, *124*(4), 2210–2234.

Cheng, C.-P., & Houze, R. A. (1979). The distribution of convective and mesoscale precipitation in gate radar echo patterns. *Monthly Weather Review*, *107*(10), 1370–1381.

Cui, W., Dong, X., Xi, B., Feng, Z., & Fan, J. (2020). Can the gpm imerg final product accurately represent mcs precipitation characteristics over the central and eastern united states? *Journal of Hydrometeorology*, *21*(1), 39–57.

Cui, W., Dong, X., Xi, B., & Liu, M. (2020). Cloud and precipitation properties of mcss along the meiyu frontal zone in central and southern china and their associated large-scale environments. *Journal of Geophysical Research: Atmospheres*, *125*(6), e2019JD031601.

Curio, J., Chen, Y., Schiemann, R., Turner, A. G., Wong, K. C., Hodges, K., & Li, Y. (2018). Comparison of a manual and an automated tracking method for tibetan plateau vortices. *Advances in Atmospheric Sciences*, *35*(8), 965–980.

Curio, J., Schiemann, R., Hodges, K. I., & Turner, A. G. (2019). Climatology of tibetan plateau vortices in reanalysis data and a high-resolution global climate model. *Journal of Climate*, *32*(6), 1933–1950.

Dai, Y., Chen, D., Yao, T., & Wang, L. (2020). Large lakes over the tibetan plateau may boost snow downwind: implications for snow disaster. *Science Bulletin*.

Diaz, M., & Boos, W. R. (2019). Barotropic growth of monsoon depressions. *Quarterly Journal of the Royal Meteorological Society*, *145*(719), 824–844.

Duan, Y., Wilson, A. M., & Barros, A. P. (2015). Scoping a field experiment: Error diagnostics of trmm precipitation radar estimates in complex terrain as a basis for iphex2014. *Hydrology and Earth System Sciences*, *19*(3), 1501–1520.

Esmaili, R. B., Tian, Y., Vila, D. A., & Kim, K.-M. (2016). A lagrangian analysis of cold cloud clusters and their life cycles with satellite observations. *Journal of Geophysical Research: Atmospheres*, *121*(19), 11–723.

Feidas, H. (2017). Satellite-observed features of a mesoscale convective complex over se europe. *International Journal of Remote Sensing*, *38*(22), 6219–6246.

Feng, X., Liu, C., Fan, G., & Zhang, J. (2017). Analysis of the structure of different tibetan plateau vortex types. *Journal of Meteorological Research*, *31*(3), 514–529.

Feng, Z., Leung, L. R., Houze Jr, R. A., Hagos, S., Hardin, J., Yang, Q., ... Fan, J. (2018). Structure and evolution of mesoscale convective systems: Sensitivity to cloud microphysics in convection-permitting simulations over the united states. *Journal of Advances in Modeling Earth Systems*, *10*(7), 1470–1494.

Feng, Z., Leung, R., Liu, N., Wang, J., Houze, R., Li, J., ... Guo, J. (2021). A global high-resolution mesoscale convective system database using satellite-derived cloud tops, surface precipitation, and tracking. *Journal of Geophysical Research: Atmospheres*, e2020JD034202.

Fitzpatrick, R. G., Parker, D. J., Marsham, J. H., Rowell, D. P., Guichard, F. M., Taylor, C. M., ... others (2020). What drives the intensification of mesoscale convective systems over the west african sahel under climate change? *Journal of Climate*, *33*(8), 3151–3172.

Flohn, H., & Reiter, E. R. (1968). Contributions to a meteorology of the tibetan highlands. *Atmospheric science paper; no. 130*.

Fritsch, J., Kane, R., & Chelius, C. (1986). The contribution of mesoscale convective weather systems to the warm-season precipitation in the united states. *Journal of climate and applied meteorology*, *25*(10), 1333–1345.

Gaál, L., Molnar, P., & Szolgay, J. (2014). Selection of intense rainfall events based on intensity thresholds and lightning data in switzerland. *Hydrology and Earth System Sciences*, *18*(5), 1561–1573.

Guo, Z.-y., Dai, X.-y., Wu, J.-p., & Lin, H. (2006). Analysis of mesoscale convective systems over tibetan plateau in summer. *Chinese Geographical Science*, *16*(2), 116–121.

Heikenfeld, M., Marinescu, P. J., Christensen, M., Watson-Parris, D., Senf, F., Van Den Heever, S. C., & Stier, P. (2019). tobac v1. 0: towards a flexible framework for tracking and analysis of clouds in diverse datasets. *Geoscientific Model Development Discussions*.

Hersbach, H., Bell, B., Berrisford, P., Hirahara, S., Horányi, A., Muñoz-Sabater, J., ... others (2020). The era5 global reanalysis. *Quarterly Journal of the Royal Meteorological Society*, *146*(730), 1999–2049.

Hitchcock, S. M., Schumacher, R. S., Herman, G. R., Coniglio, M. C., Parker, M. D., & Ziegler, C. L. (2019). Evolution of pre-and postconvective environmental profiles from mesoscale convective systems during pecan. *Monthly Weather Review*, *147*(7), 2329–2354.

Houze, R. A., Wilton, D. C., & Smull, B. F. (2007). Monsoon convection in the himalayan region as seen by the trmm precipitation radar. *Quarterly Journal of the Royal Meteorological Society: A journal of the atmospheric sciences, applied meteorology and physical oceanography*, *133*(627), 1389–1411.

Houze Jr, R. A. (2004). Mesoscale convective systems. *Reviews of Geophysics*, *42*(4).

Hu, H., Leung, R., & Feng, Z. (2020). Observed warm-season characteristics of mcs and non-mcs rainfall and their recent changes in the central united states. *Geophysical Research Letters*, *47*(6), e2019GL086783.

Huang, X., Hu, C., Huang, X., Chu, Y., Tseng, Y.-h., Zhang, G. J., & Lin, Y. (2018). A long-term tropical mesoscale convective systems dataset based on a novel objective automatic tracking algorithm. *Climate dynamics*, *51*(7), 3145–3159.

Huffman, G., Stocker, E., Bolvin, D., Nelkin, E., & Jackson, T. (2019). Gpm imerg final precipitation l3 half hourly 0.1 degree x 0.1 degree v06. *Greenbelt, MD, Goddard Earth Sciences Data and Information Services Center (GES DISC)*.

Hunt, K., Curio, J., Turner, A., & Schiemann, R. (2018). Subtropical westerly jet influence on occurrence of western disturbances and tibetan plateau vortices.

Geophysical Research Letters, *45*(16), 8629–8636.
Hurley, J. V., & Boos, W. R. (2015). A global climatology of monsoon low-pressure systems. *Quarterly Journal of the Royal Meteorological Society*, *141*(689), 1049–1064.
Janowiak, J., Joyce, B., & Xie, P. (2017). Ncep/cpc l3 half hourly 4km global (60s - 60n) merged ir v1. *Edited by Andrey Savtchenko, Greenbelt, MD, Goddard Earth Sciences Data and Information Services Center (GES DISC).*
Jia, X., & Yang, S. (2013). Impact of the quasi-biweekly oscillation over the western north pacific on east asian subtropical monsoon during early summer. *Journal of Geophysical Research: Atmospheres*, *118*(10), 4421–4434.
Jiang, J.-x., & Fan, M.-z. (2002). Convective clouds and mesoscale convective systems over the tibetan plateau in summer. *Chin. J. Atmos. Sci*, *26*(2), 263–270.
Kirkpatrick, C., McCaul Jr, E. W., & Cohen, C. (2011). Sensitivities of simulated convective storms to environmental cape. *Monthly weather review*, *139*(11), 3514–3532.
Klein, C., Belušić, D., & Taylor, C. M. (2018). Wavelet scale analysis of mesoscale convective systems for detecting deep convection from infrared imagery. *Journal of Geophysical Research: Atmospheres*, *123*(6), 3035–3050.
Kukulies, J., Chen, D., & Wang, M. (2019). Temporal and spatial variations of convection and precipitation over the tibetan plateau based on recent satellite observations. part i: Cloud climatology derived from cloudsat and calipso. *International Journal of Climatology*, *39*(14), 5396–5412.
Kukulies, J., Chen, D., & Wang, M. (2020). Temporal and spatial variations of convection, clouds and precipitation over the tibetan plateau from recent satellite observations. part ii: Precipitation climatology derived from global precipitation measurement mission. *International Journal of Climatology*.
Lai, H.-W., Chen, H. W., Kukulies, J., Ou, T., & Chen, D. (2021). Regionalization of seasonal precipitation over the tibetan plateau and associated large-scale atmospheric systems. *Journal of Climate*, *34*(7), 2635–2651.
Li, L., Zhang, R., Wen, M., & Liu, L. (2014). Effect of the atmospheric heat source on the development and eastward movement of the tibetan plateau vortices. *Tellus A: Dynamic Meteorology and Oceanography*, *66*(1), 24451.
Li, P., Moseley, C., Prein, A. F., Chen, H., Li, J., Furtado, K., & Zhou, T. (2020). Mesoscale convective system precipitation characteristics over east asia. part i: regional differences and seasonal variations. *Journal of Climate*, *33*(21), 9271–9286.
Li, Y., Yun, W., Yang, S., Liang, H., Shouting, G., & Fu. (2008). Characteristics of summer convective systems initiated over the tibetan plateau. part i: Origin, track, development, and precipitation. *Journal of applied meteorology and climatology*, *47*(10), 2679–2695.
Ma, Y., Tang, G., Long, D., Yong, B., Zhong, L., Wan, W., & Hong, Y. (2016). Similarity and error intercomparison of the gpm and its predecessor-trmm multisatellite precipitation analysis using the best available hourly gauge network over the tibetan plateau. *Remote sensing*, *8*(7), 569.
Maddox, R. A. (1980). Mesoscale convective complexes. *Bulletin of the American Meteorological Society*, 1374–1387.
Mai, Z., Fu, S.-M., Sun, J.-H., Hu, L., & Wang, X.-m. (2021). Key statistical characteristics of the mesoscale convective systems generated over the tibetan plateau and their relationship to precipitation and southwest vortices. *International Journal of Climatology*, *41*, E875–E896.
Morel, C., & Senesi, S. (2002). A climatology of mesoscale convective systems over europe using satellite infrared imagery. ii: Characteristics of european mesoscale convective systems. *Quarterly Journal of the Royal Meteorological Society: A journal of the atmospheric sciences, applied meteorology and*

physical oceanography, *128*(584), 1973–1995.

Orlanski, I. (1975). A rational subdivision of scales for atmospheric processes. *Bulletin of the American Meteorological Society*, 527–530.

Ou, T., Chen, D., Chen, X., Lin, C., Yang, K., Lai, H.-W., & Zhang, F. (2020). Simulation of summer precipitation diurnal cycles over the tibetan plateau at the gray-zone grid spacing for cumulus parameterization. *Climate Dynamics*, *54*(7), 3525–3539.

Prein, A., Liu, C., Ikeda, K., Bullock, R., Rasmussen, R. M., Holland, G. J., & Clark, M. (2017). Simulating north american mesoscale convective systems with a convection-permitting climate model. *Climate Dynamics*, 1–16.

Rasmussen, K., & Houze, R. (2012). A flash-flooding storm at the steep edge of high terrain: disaster in the himalayas. *Bulletin of the American Meteorological Society*, *93*(11), 1713–1724.

Redelsperger, J.-L., Diongue, A., Diedhiou, A., Ceron, J.-P., Diop, M., Gueremy, J.-F., & Lafore, J.-P. (2002). Multi-scale description of a sahelian synoptic weather system representative of the west african monsoon. *Quarterly Journal of the Royal Meteorological Society: A journal of the atmospheric sciences, applied meteorology and physical oceanography*, *128*(582), 1229–1257.

Ren, X., Yang, D., & Yang, X.-Q. (2015). Characteristics and mechanisms of the subseasonal eastward extension of the south asian high. *Journal of Climate*, *28*(17), 6799–6822.

Roebber, P. J., Schultz, D. M., & Romero, R. (2002). Synoptic regulation of the 3 may 1999 tornado outbreak. *Weather and Forecasting*, *17*(3), 399–429.

Romatschke, U., Medina, S., & Houze, R. (2010). Regional, seasonal, and diurnal variations of extreme convection in the south asian region. *Journal of climate*, *23*(2), 419–439.

Rossow, W. B., & Schiffer, R. A. (1999). Advances in understanding clouds from isccp. *Bulletin of the American Meteorological Society*, *80*(11), 2261–2288.

Rutledge, S. A., & Houze Jr, R. A. (1987). A diagnostic modelling study of the trailing stratiform region of a midlatitude squall line. *Journal of the atmospheric sciences*, *44*(18), 2640–2656.

Schädlich, S., Göttsche, F., & Olesen, F.-S. (2001). Influence of land surface parameters and atmosphere on meteosat brightness temperatures and generation of land surface temperature maps by temporally and spatially interpolating atmospheric correction. *Remote Sensing of Environment*, *75*(1), 39–46.

Schiemann, R., Lüthi, D., & Schär, C. (2009). Seasonality and interannual variability of the westerly jet in the tibetan plateau region. *Journal of climate*, *22*(11), 2940–2957.

Shang, W., Ren, X., Huang, B., Cubasch, U., & Yang, X.-Q. (2019). Subseasonal intensity variation of the south asian high in relationship to diabatic heating: observation and cmip5 models. *Climate Dynamics*, *52*(3), 2413–2430.

Shi, X., Wang, Y., & Xu, X. (2008). Effect of mesoscale topography over the tibetan plateau on summer precipitation in china: A regional model study. *Geophysical Research Letters*, *35*(19).

Song, F., Feng, Z., Leung, L. R., Houze Jr, R. A., Wang, J., Hardin, J., & Homeyer, C. R. (2019). Contrasting spring and summer large-scale environments associated with mesoscale convective systems over the us great plains. *Journal of Climate*, *32*(20), 6749–6767.

Sugimoto, S., & Ueno, K. (2012). Role of mesoscale convective systems developed around the eastern tibetan plateau in the eastward expansion of an upper tropospheric high during the monsoon season. *Journal of the Meteorological Society of Japan. Ser. II*, *90*(2), 297–310.

Talib, J., Taylor, C. M., Duan, A., & Turner, A. G. (2021). Intraseasonal soil moisture–atmosphere feedbacks on the tibetan plateau circulation. *Journal of Climate*, *34*(5), 1789–1807.

Tao, S.-y., & Ding, Y.-h. (1981). Observational evidence of the influence of the qinghai-xizang (tibet) plateau on the occurrence of heavy rain and severe convective storms in china. *Bulletin of the American Meteorological Society*, *62*(1), 23–30.

Vondou, D. A., Nzeukou, A., & Kamga, F. M. (2010). Diurnal cycle of convective activity over the west of central africa based on meteosat images. *International journal of applied earth observation and geoinformation*, *12*, S58–S62.

Wang, B. (1987). The development mechanism for tibetan plateau warm vortices. *Journal of the atmospheric sciences*, *44*(20), 2978–2994.

Wang, C., Luo, J., Rossow, W. B., & Pearl, C. (2018). Production of globally uniform isccp convection tracking (ct) dataset and preliminary analysis results. *AGUFM*, *2018*, A11J–2361.

Wen, Y., Behrangi, A., Lambrigtsen, B., & Kirstetter, P.-E. (2016). Evaluation and uncertainty estimation of the latest radar and satellite snowfall products using snotel measurements over mountainous regions in western united states. *Remote Sensing*, *8*(11), 904.

Xiang, S., Li, Y., Li, D., & Yang, S. (2013). An analysis of heavy precipitation caused by a retracing plateau vortex based on trmm data. *Meteorology and Atmospheric Physics*, *122*(1-2), 33–45.

Xu, R., Tian, F., Yang, L., Hu, H., Lu, H., & Hou, A. (2017). Ground validation of gpm imerg and trmm 3b42v7 rainfall products over southern tibetan plateau based on a high-density rain gauge network. *Journal of Geophysical Research: Atmospheres*, *122*(2), 910–924.

Xu, W., & Zipser, E. J. (2011). Diurnal variations of precipitation, deep convection, and lightning over and east of the eastern tibetan plateau. *Journal of Climate*, *24*(2), 448–465.

Yang, R., Zhang, Y., Sun, J., Fu, S., & Li, J. (2019). The characteristics and classification of eastward-propagating mesoscale convective systems generated over the second-step terrain in the yangtze river valley. *Atmospheric Science Letters*, *20*(1), e874.

Yao, T., Xue, Y., Chen, D., Chen, F., Thompson, L., Cui, P., … others (2019). Recent third pole's rapid warming accompanies cryospheric melt and water cycle intensification and interactions between monsoon and environment: Multidisciplinary approach with observations, modeling, and analysis. *Bulletin of the American Meteorological Society*, *100*(3), 423–444.

Yasunari, T., & Miwa, T. (2006). Convective cloud systems over the tibetan plateau and their impact on meso-scale disturbances in the meiyu/baiu frontal zone. *Journal of the Meteorological Society of Japan. Ser. II*, *84*(4), 783–803.

Ye, D.-Z., & Wu, G.-X. (1998). The role of the heat source of the tibetan plateau in the general circulation. *Meteorology and Atmospheric Physics*, *67*(1-4), 181–198.

Yuan, J., & Houze, R. (2010). Global variability of mesoscale convective system anvil structure from a-train satellite data. *Journal of Climate*, *23*(21), 5864–5888.

Zhang, L., Su, F., Yang, D., Hao, Z., & Tong, K. (2013). Discharge regime and simulation for the upstream of major rivers over tibetan plateau. *Journal of Geophysical Research: Atmospheres*, *118*(15), 8500–8518.

Zhang, S., Wang, D., Qin, Z., Zheng, Y., & Guo, J. (2018). Assessment of the gpm and trmm precipitation products using the rain gauge network over the tibetan plateau. *Journal of Meteorological Research*, *32*(2), 324–336.

Zheng, Y., Chen, J., & Zhu, P. (2008). Climatological distribution and diurnal variation of mesoscale convective systems over china and its vicinity during summer. *Chinese Science Bulletin*, *53*(10), 1574–1586.

Zhou, X., Yang, K., Ouyang, L., Wang, Y., Jiang, Y., Li, X., … Prein, A. (2021). Added value of kilometer-scale modeling over the third pole region: a cordex-

1333 cptp pilot study. *Climate Dynamics*, 1–15.